

Projected Density Matrix Sampling for Lattice Hamiltonians

Abhishek Karna ^{1,*} Hansen S. Wu ^{2,†} Shailesh Chandrasekharan ^{1,‡} and Ribhu K. Kaul ^{2,§}

¹*Department of Physics, Duke University, Box 90305, Durham, North Carolina 27708, USA*

²*Department of Physics, Pennsylvania State University, State College, Pennsylvania 16801, USA*

(Dated: December 16, 2025)

Quantum Monte Carlo methods are powerful tools for studying quantum many-body systems but face difficulties in accessing excited states and in treating sign problems. We present a continuous-time path-integral Monte Carlo method for computing the low-lying spectrum of generic quantum Hamiltonians within a projection subspace. The method projects the thermal density matrix onto a subspace spanned by a chosen set of linearly independent states. It is free of Trotter discretization errors and systematically converges to the low-energy states which have finite overlap with the projection subspace as the β parameter increases. While most effective for systems without a sign problem, the method also yields information about low-energy spectra when sign problems are present. We illustrate the approach on two problems. For the sign-free case, we compute the first four low-energy levels in the scaling limit of the one-dimensional Ising model with both transverse and longitudinal fields, demonstrating the flow from the conformal limit to the massive E_8 quantum field theory. For the sign-problem case, we apply the method to the frustrated Shastry–Sutherland model and benchmark it against exact diagonalization on small lattices. We also present results for larger systems beyond the lattice sizes accessible to exact diagonalization, while limited to small β where sign problems occur. Our method provides a general route toward quantum Monte Carlo spectroscopy for lattice Hamiltonians.

I. INTRODUCTION

Computing the low-lying spectrum of quantum Hamiltonians is a central challenge in many-body physics and remains an active area of research across fields ranging from condensed matter to nuclear and particle physics. With the recent surge of interest in using quantum computers to solve generic quantum problems, alternative classical methods that can benchmark and cross-check quantum results are particularly valuable. While tensor networks are the main tools used today for such cross-verification [1], Monte Carlo sampling also provides a powerful framework for addressing these problems. However, its applicability is often limited by the notorious sign problem, which, in its most general form, is computationally hard [2]. The severity of the sign problem depends on several factors, including the details of the interactions, the choice of Hilbert-space basis used for Monte Carlo sampling, and the energy subspace being accessed. A variety of strategies have been explored to mitigate it in specific cases [3–5].

The fundamental difficulty arises because the full Hilbert space of a quantum system typically grows exponentially with system size which makes it hard to efficiently isolate the relevant low-energy subspace. A common approach begins with the thermal density matrix, $\rho = e^{-\beta H}$, which naturally suppresses high-energy contributions and projects onto the low-energy sector as β becomes large. In general, there is no simple basis [s] in

which all matrix elements $\rho_{s_f, s_i} = \langle s_f | e^{-\beta H} | s_i \rangle$ can be expressed as a sum over positive weights, so that Monte Carlo sampling becomes possible. This is the origin of the sign problem.

A related idea that has not been explored as extensively, and which serves as the main motivation for this work, is to project the thermal density matrix onto a carefully chosen d_{proj} -dimensional *projection subspace* \mathbb{P} , spanned by a set of linearly independent *projection states* $|\psi_a\rangle$ ($a = 1, 2, \dots, d_{\text{proj}}$) within the Hilbert space. We then define the $d_{\text{proj}} \times d_{\text{proj}}$ matrix-valued partition function Z as the *projected thermal density matrix*, whose elements are given by

$$Z_{ac} = \langle \psi_a | e^{-\beta H} | \psi_c \rangle. \quad (1)$$

Similarly, we define the corresponding *projected thermal energy matrix* E in the same subspace, with matrix elements

$$E_{ac} = \langle \psi_a | H e^{-\beta H} | \psi_c \rangle. \quad (2)$$

The d_{proj} eigenvalues $e_a(\beta)$ of the matrix product EZ^{-1} are referred to as the *projected thermal energies* of H , which depend on the chosen projection subspace.

The thermal energies $e_a(\beta)$ depend on the inverse temperature β and converge, in the zero temperature limit, to what we refer to as the *projected low-energy spectrum* of H . It can be shown, using standard linear-algebraic arguments, that this spectrum corresponds to the d_{proj} lowest eigenvalues of H whose eigenstates not only have nonzero overlap with the projection subspace but also remain linearly independent after being projected onto it.

This broad idea of extracting the low-energy spectrum using Monte Carlo techniques is well known in the lattice field theory community and is often discussed within the

* abhishek.karna@duke.edu

† hsw5129@psu.edu

‡ sch27@duke.edu

§ ribhu.kaul@psu.edu

framework of the generalized eigenvalue problem [6]. It is extensively employed to determine low-energy particle spectra [7–10]. Similar approaches have been proposed for constructing the reduced density matrix through a spatial bipartition for use in Monte Carlo simulations, and applied to compute entanglement entropy [11] and to extract entanglement level spectra in model quantum systems [12, 13]. However, its applicability to a broad range of problems—particularly in condensed matter physics and in the Hamiltonian framework in the above form—has not yet been systematically explored. For instance, if the projection subspace coincides exactly with an energy subspace of the Hamiltonian, accurate results for the low-energy spectrum can be obtained using efficient algorithms even for arbitrarily small values of β , irrespective of whether the problem suffers from a sign problem [14]. Furthermore, by judiciously enlarging the projection subspace, the β -dependence of the extracted energies can be exponentially suppressed when accurate Monte Carlo sampling is feasible [6]. These insights, however, have not yet been effectively applied widely to physically interesting systems, like quantum spin models and qubit regularized Hamiltonians [15].

The goal of this work is to systematically investigate and develop the idea of sampling the thermal density matrix in a projection subspace in substantial detail. To that end, we introduce the Projected Density Matrix Sampling (PDMS) method with the aim of computing the projected thermal energies $e_a(\beta)$ for generic quantum Hamiltonians. Our algorithm samples configurations that contribute to the density matrix, expressed in the path-integral representation, directly in continuous time, thereby eliminating errors typically introduced by Trotter decompositions. All matrix elements of Z and E are computed as observables in the Monte Carlo procedure, up to an overall normalization factor that cancels when evaluating EZ^{-1} to extract $e_a(\beta)$. Sign problems, if present, are incorporated into the observables in the usual manner.

Our work synthesizes several established ideas, including continuous-time path-integral formulations [16–18], the stochastic series expansion [19–21], worm and loop algorithms [14, 22, 23], and meron-cluster techniques [24]. To illustrate the method, we apply it to two representative problems: (1) the one-dimensional Transverse Field Ising Model (TFIM) in the presence of a small longitudinal magnetic field. Here, we demonstrate how our method can compute the low-lying mass spectrum of the E_8 quantum field theory that is known to emerge in this regime [25]. And, (2) the Shastry–Sutherland model (SSM) [26], a paradigmatic frustrated antiferromagnetic system with a severe sign problem but of great interest in condensed matter physics, owing to its exotic phase diagram and experimental relevance (see Ref. [27] and references therein). In this case, our goal is to investigate how well our algorithm computes the values of $e_a(\beta)$ on small lattices for selected projection subspaces. These thermal energies can be obtained independently using exact diagonalization for comparison. We hope that these two distinct applica-

tions of our method, along with previous developments in similar directions, help convey its broad applicability across nuclear, particle, and condensed matter physics.

The rest of the paper is organized as follows. In Section II, we describe our general formalism of representing the thermal density matrix in a continuous-time path-integral form and discuss the bookkeeping of the signs. In Section III, we detail the two update algorithms for our Monte Carlo: (i) the link update and (ii) the spin update. Various details about leveraging the properties of different configuration representations and computation of the $d_{\text{proj}} \times d_{\text{proj}}$ projected thermal matrices Z and E are also discussed therein. As can be anticipated, the role of the choice of the projection subspace is crucial in our approach. We discuss this in Section IV by providing a linear algebraic description of the algorithmic process towards convergence to the low-energy spectrum for a generic quantum Hamiltonian H . We also comment on rates of convergence and potential solutions to the complications associated in models with sign problems. In Section V, we apply our algorithm to the 1D-TFIM at criticality in the presence of magnetic field and obtain the first two predicted mass ratios of the associated E_8 massive quantum field theory. Similarly, in Section VI, we explore the 2D-frustrated SSM Hamiltonian and demonstrate the effectiveness of different projection subspaces at different coupling ratios. We also discuss strategies for improving the convergence by either enlarging the dimension of the projection subspace d_{proj} or choosing an optimal projection basis, thereby partially mitigating the sign problem. We summarize our discussions in Section VII.

II. THERMAL DENSITY MATRIX IN CONTINUOUS TIME

To construct a Monte Carlo sampling procedure for the thermal density matrix, we formulate it in a continuous-time path-integral representation.¹ We focus on Hamiltonians that can be written in the generic form

$$H = \sum_{\ell} H_{\ell} + E_0, \quad (3)$$

where ℓ labels a bond associated with local interactions, and H_{ℓ} denotes the Hamiltonian corresponding to the interaction on that bond. In the two applications considered in this work, ℓ corresponds to interactions between two lattice sites; however, in general, ℓ can involve interactions among multiple sites, such as those encountered in

¹ While we formulate the algorithm in the path integral representation, our ideas for computing the Z and H matrices and using them to extract the low lying states can clearly equally well be formulated in the popular stochastic series expansion representation [19]. This is outlined in App. A.

lattice gauge theories. The constant E_0 is chosen so that the diagonal matrix elements of H_ℓ are zero or negative in the chosen basis.

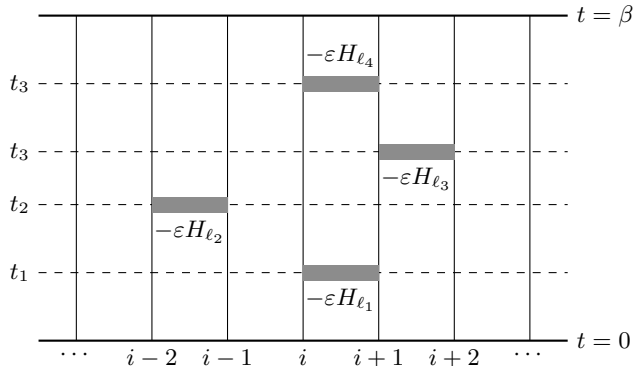


FIG. 1. Illustration of a continuous-time path-integral configuration $[\ell]$, introduced in Eq. (6), for a nearest-neighbor Hamiltonian in one spatial dimension. The configuration shown contains $N_\ell = 4$ bond operators $(-\varepsilon H_{\ell_i})$ at times t_i ($i = 1, 2, 3, 4$). Each operator is accompanied by a factor ε , representing the continuous-time measure dt , which cancels naturally during updates enforcing detailed balance. The full configuration $[\ell, s]$ is obtained by inserting complete sets of spin states, as explained in Eq. (8).

The thermal density matrix is defined by the matrix element

$$\rho_{s_f, s_i} = \langle s_f | e^{-\beta H} | s_i \rangle = \langle s_f | \underbrace{e^{-\varepsilon H} \cdots e^{-\varepsilon H}}_{L_t \text{ terms}} | s_i \rangle, \quad (4)$$

where the standard Trotter decomposition is introduced with L_t time slices and temporal lattice spacing ε , such that $\beta = \varepsilon L_t$. As we explain in the next section, we can take the limit $\varepsilon \rightarrow 0$ and $L_t \rightarrow \infty$ in our method. In this limit we can expand each short-time exponential to leading order as

$$e^{-\varepsilon H} \simeq \left(1 - \varepsilon \sum_{\ell} H_{\ell} \right) e^{-\varepsilon E_0} + \mathcal{O}(\varepsilon^2). \quad (5)$$

Substituting this into the Trotterized expression gives

$$\rho_{s_f, s_i} = e^{-\beta E_0} \sum_{[\ell]} \langle s_f | (-\varepsilon H_{\ell_{N_\ell}}) \cdots (-\varepsilon H_{\ell_2}) (-\varepsilon H_{\ell_1}) | s_i \rangle, \quad (6)$$

where $[\ell]$ denotes a continuous-time configuration consisting of an ordered sequence of N_ℓ bond operators inserted at imaginary times $t_1 < t_2 < \cdots < t_{N_\ell}$. We refer to $[\ell]$ as the link configuration. An illustration of such a configuration for a one-dimensional lattice system with nearest-neighbor interactions is shown in Fig. 1. The TFIM studied in this work features link configurations of this type, whereas the Shastry-Sutherland Model (SSM) includes bond operators involving both nearest-neighbor and diagonal sites.

The path integral is formulated in a complete basis of the local Hilbert space, defined by the expression

$$I = \sum_s |s\rangle \langle s|. \quad (7)$$

We will refer to s in the above expression as ‘‘spins,’’ although they may represent any discrete set of quantum numbers. Inserting Eq. (7) between successive bond operators, we obtain the full path-integral expression

$$\begin{aligned} \rho_{s_f, s_i} &= e^{-\beta E_0} \sum_{[\ell, s]} \langle s_f | (-\varepsilon H_{\ell_{N_\ell}}) | s_{N_\ell-1} \rangle \langle s_{N_\ell-1} | \cdots \\ &\quad \cdots | s_{t_2} \rangle \langle s_{t_2} | (-\varepsilon H_{\ell_2}) | s_{t_1} \rangle \langle s_{t_1} | (-\varepsilon H_{\ell_1}) | s_i \rangle, \\ &= e^{-\beta E_0} \sum_{[\ell, s]} W([\ell, s]), \end{aligned} \quad (8)$$

where the sum now extends over both the link configurations $[\ell]$ and the intermediate spin states $[s]$, subject to the fixed boundary conditions s_i and s_f . The combined configuration $[\ell, s]$ carries a weight $W([\ell, s])$, which is given by the product of local matrix elements of the form $\langle s_t | (-\varepsilon H_{\ell_t}) | s_{t-1} \rangle$. If all local matrix elements are positive, $W([\ell, s])$ is positive, and one can directly design a Monte Carlo algorithm to sample configurations $[\ell, s]$ with this weight. With a suitable choice of E_0 , this positivity can be ensured for diagonal elements.

However, off-diagonal elements may still be negative, rendering $W([\ell, s])$ sign-indefinite. To address this, we define a modified Hamiltonian H_ℓ^b by

$$(-\varepsilon H_\ell^b) = |-\varepsilon H_\ell|, \quad (9)$$

so that all matrix elements are nonnegative. Using this definition, we sample configurations according to the probability distribution

$$P([\ell, s]) = \rho_{s_f, s_i}^b / Z^b, \quad (10)$$

where

$$\begin{aligned} \rho_{s_f, s_i}^b &= e^{-\beta E_0} \langle s_f | (-\varepsilon H_{\ell_k}^b) \cdots (-\varepsilon H_{\ell_2}^b) (-\varepsilon H_{\ell_1}^b) | s_i \rangle \\ &= e^{-\beta E_0} \sum_{[\ell, s]} W^b([\ell, s]), \end{aligned} \quad (11)$$

and the normalization

$$Z^b = \sum_{s_i, s_f} \rho_{s_f, s_i}^b \quad (12)$$

serves as the sampling partition function.

The effect of the original signs is restored through a sign factor $\mathcal{S}([\ell, s])$, defined as the product of the local signs of the matrix elements,

$$W([\ell, s]) = \mathcal{S}([\ell, s]) W^b([\ell, s]). \quad (13)$$

The thermal density matrix can then be expressed as

$$\rho_{s_f, s_i} = Z^b \langle \mathcal{S}([\ell, s]) \rangle, \quad (14)$$

where the expectation value is evaluated as a Monte Carlo average over configurations $[\ell, s]$ sampled with weight $W^b([\ell, s])$ and fixed boundary states s_i and s_f .

III. THE MONTE CARLO ALGORITHM

In this section, we summarize the two Monte Carlo updates used to generate the path-integral configurations $[\ell, s]$ discussed above. We refer to these as (i) the link update and (ii) the spin update. We conclude the section by explaining how the sampled configurations are used to compute the Z and E matrices introduced in Eqs. (1) and (2) as observables.

A. Link update

The link update modifies the space-time locations of the link operators in the configuration $[\ell]$. Following the idea of the stochastic series expansion (SSE) algorithm [19], only diagonal link operators are inserted or removed during this update. A typical proposal (chosen with probability 1/2) is either to add a new diagonal link operator or to remove an existing one. To add a link, a random spatial location (chosen uniformly among V sites) and a random time slice at that location (chosen uniformly among L_t slices) are selected, and one of the d_ℓ possible diagonal operators that can be inserted at that location is proposed. To remove a link, a random spatial location (chosen uniformly among V sites) is selected, and one of the n_ℓ existing diagonal links at that location (across all time slices) is chosen uniformly and proposed for deletion. Each proposal is then accepted or rejected according to the Metropolis criterion, ensuring detailed balance.

To illustrate, let W_i be the weight of the initial configuration and W_f that of the proposed configuration obtained by adding a diagonal bond with matrix element $\varepsilon w = \langle s_{t_k} | (-\varepsilon H_{\ell_k}^b) | s_{t_k-1} \rangle$. This implies $W_f = W_i(\varepsilon w)$. If the number of diagonal links at the chosen location is n_ℓ , it changes to $n_\ell + 1$ after insertion. The forward and reverse proposal probabilities (excluding the Metropolis acceptance factor) are then proportional to

$$q_{i \rightarrow f} = \frac{1}{2} \frac{1}{V} \frac{1}{L_t}, \quad q_{f \rightarrow i} = \frac{1}{2} \frac{1}{V} \frac{1}{(n_\ell + 1)}. \quad (15)$$

Detailed balance gives the Metropolis acceptance probability

$$A_{i \rightarrow f} = \min \left(1, \frac{q_{f \rightarrow i} W_f}{q_{i \rightarrow f} W_i} \right), \quad (16)$$

and similarly for the reverse move. Because $W_f/W_i = (\varepsilon w)$ and $q_{f \rightarrow i}/q_{i \rightarrow f} = L_t/(n_\ell + 1)$, the acceptance probabilities depend only on $\beta = \varepsilon L_t$. This demonstrates that the algorithm possesses a smooth continuous-time limit, allowing us to impose $\varepsilon \rightarrow 0$ and $L_t \rightarrow \infty$.

In practice, when implementing the algorithm, we set $\varepsilon \approx 10^{-8}$ (or smaller) and use a large number of time slices, $L_t = \beta/\varepsilon$. In this discrete-time approach, if a link already exists at the chosen time slice when a new link is proposed for insertion, no additional link is added. However, such occurrences become vanishingly rare as

ε decreases further. It is also worth noting that the memory requirements do not scale with L_t , since only the locations of the N_ℓ bonds in the configuration $[\ell, s]$ need to be stored, and this number scales with the physical space-time volume $V\beta$.

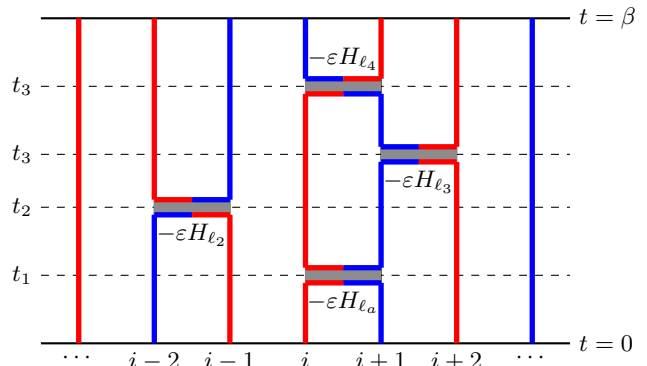


FIG. 2. The loop-cluster configuration $[\ell, s]$ associated with the continuous-time path-integral configuration $[\ell]$ shown in Fig. 1. The two colors represent opposite spins.

B. Spin update

The spin update keeps the space-time locations of the link operators $(-\varepsilon H_\ell)$ fixed and updates the spin configuration $[s]$ in a manner consistent with the matrix elements of these operators. Several efficient methods now exist to implement changes to $[s]$ while maintaining detailed balance, including cluster updates [23], worm updates [22], and loop updates [28].

In some cases, spin configurations can be reorganized into correlated clusters. For example, in the SSM, nonzero matrix elements of the bond Hamiltonian always connect opposite spins on neighboring sites in the bra and ket states. This allows for the well known cluster representation of the spins [29]. Imposing this restriction on the link configuration in Fig. 1 generates the corresponding cluster configuration of spins, as illustrated in Fig. 2. In our work, we employ such cluster representations, together with the meron-cluster approach [24], to partially alleviate some of the sign problems associated with the SSM.

C. Computation of Z and E matrices

Each new $[\ell, s]$ configuration is generated from an old $[\ell, s]$ configuration after a single sweep, which consists of a sequence of link updates followed by a sequence of spin updates. The numbers of link and spin updates in each sweep are chosen such that all bond operators have a reasonable probability of being updated during the sweep. The quoted results are obtained from statistics of sampled $[\ell, s]$ configurations generated over a few billion sweeps. We typically average observables over subsets of these

configurations to construct thousands of data sets and then perform a bootstrap analysis over these averaged data sets to estimate the mean values and statistical errors.

Our observables are the projected thermal density matrix Z and the projected thermal energy matrix E , defined in Eqs. (1) and (2). These quantities can be estimated as Monte Carlo averages using the wavefunctions $\psi_a(s) = \langle s | \psi_a \rangle$ of the projection states. One obtains

$$\frac{Z_{ac}}{Z^b} = \langle \mathcal{S}([\ell, s]) \psi_a(s_f) \psi_c(s_i) \rangle_{W^b}, \quad (17)$$

$$\frac{\tilde{E}_{ac}}{Z^b} = -\frac{1}{\beta} \langle N_\ell \mathcal{S}([\ell, s]) \psi_a(s_f) \psi_c(s_i) \rangle_{W^b}, \quad (18)$$

where $\langle \cdot \rangle_{W^b}$ denotes an average over configurations sampled with weight $W^b([\ell, s])$. The sign factor $\mathcal{S}([\ell, s])$, introduced earlier in Section II, corrects for the modified sampling weight. It is straightforward to verify that

$$EZ^{-1} = \tilde{E}Z^{-1} + E_0, \quad (19)$$

and that the common normalization factor Z^b cancels in this calculation.

IV. CHOICE OF THE PROJECTION SUBSPACE

The choice of the projection subspace is a crucial step in the successful application of our method. This subspace determines not only the projected low-energy spectrum of H , but also the projected thermal energies $e_a(\beta)$ and the rate at which these thermal energies converge to the low-energy spectrum. We now analyze this rate of convergence quantitatively for sufficiently large values of β , where this question becomes meaningful. As we will see, the convergence is exponential in β [6].

Let us first define \mathbb{P} as the projection operator that maps the full Hilbert space onto the projection subspace. The projected thermal density matrix, in operator form, is then given by

$$\hat{Z} = \mathbb{P}e^{-\beta H}\mathbb{P},$$

whose matrix elements in the chosen projection states were specified in Eq. (1). In general, several energy eigenstates $|\alpha\rangle$ of H with energies \mathcal{E}_α will have nonzero overlap with the projection subspace. We will refer to these as the *projected energies* of H . Each of these projected energies is associated with the *projected vector* $|p_\alpha\rangle = \mathbb{P}|\alpha\rangle$ obtained by projecting $|\alpha\rangle$ onto the projection subspace. It is then straightforward to verify that

$$\hat{Z} = \sum_{\alpha} |p_\alpha\rangle e^{-\beta \mathcal{E}_\alpha} \langle p_\alpha|, \quad (20)$$

where the sum is restricted to those eigenstates of H that have a nonzero projection onto the projection subspace.

Note that the vectors $|p_\alpha\rangle$ are not necessarily orthogonal or even linearly independent. In fact, only d_{proj} of them

can be linearly independent. The central idea behind our method is that, for sufficiently large β , we can decompose Eq. (20) into two terms:

$$\hat{Z} = \sum_{a=1}^{d_{\text{proj}}} |p_{\alpha_a}\rangle e^{-\beta \mathcal{E}_{\alpha_a}} \langle p_{\alpha_a}| + \sum_{\gamma} |p_{\gamma}\rangle e^{-\beta \mathcal{E}_{\gamma}} \langle p_{\gamma}|. \quad (21)$$

The first term contains a specific set of d_{proj} linearly independent projected vectors, $\{|p_{\alpha_1}\rangle, \dots, |p_{\alpha_{d_{\text{proj}}}}\rangle\}$, which we refer to as the *projected low-energy vectors*. The second term arises from the remaining projected vectors that are linearly dependent on those in the first term. The vectors in the first term are associated with the lowest possible ordered energies $\mathcal{E}_{\alpha_1} \leq \mathcal{E}_{\alpha_2} \leq \dots \leq \mathcal{E}_{\alpha_{d_{\text{proj}}}}$ and define the *projected low-energy spectrum* introduced in Section I, which we aim to compute using our method. The projected thermal energies $e_a(\beta)$ converge to \mathcal{E}_{α_a} in the limit $\beta \rightarrow \infty$. As we will see below, this term acts as a correction that governs the rate of convergence of $e_a(\beta)$.

We begin by outlining a systematic procedure to identify the projected low-energy vectors that contribute to the first term in Eq. (21). We first construct an ordered list of all the vectors in Eq. (20) according to their energies in ascending order. Within a degenerate subspace, the order can be chosen arbitrarily as long as the original eigenvectors of H in the degenerate subspace are chosen carefully. We will come back to this point later. The first vector $|p_{\alpha_1}\rangle$ is identified as the lowest-energy vector on this ordered list. The next higher vector is identified as $|p_{\alpha_2}\rangle$ only if it is linearly independent of $|p_{\alpha_1}\rangle$; otherwise, we skip to the next higher-energy vector until an independent one is found. This process is repeated iteratively: $|p_{\alpha_k}\rangle$ is identified as the next independent vector following the first $k-1$ already identified vectors $\{|p_{\alpha_1}\rangle, |p_{\alpha_2}\rangle, \dots, |p_{\alpha_{k-1}}\rangle\}$. The search terminates once $|p_{\alpha_{d_{\text{proj}}}}\rangle$ has been identified. All remaining vectors that are skipped or not encountered during this process contribute to the second term in Eq. (21).

Each term in the degenerate subspace with a fixed low energy \mathcal{E}_{α_i} in the first term carries a suppression factor $e^{-\beta \mathcal{E}_{\alpha_i}}$. This subspace can also receive contributions from the second term, but they are always accompanied by a suppression factor $e^{-\beta \mathcal{E}_{\gamma}}$, where even the smallest \mathcal{E}_{γ} is strictly greater than \mathcal{E}_{α_i} . To ensure that $\mathcal{E}_{\gamma} > \mathcal{E}_{\alpha_i}$, the original eigenvectors of H in the degenerate subspace of energy \mathcal{E}_{α_i} must be chosen such that any projected vector from that subspace appearing in the second term of Eq. (21) has no overlap with any projected vector in the degenerate subspace of the first term. This is always possible.

With this insight, one can use Eq. (21) to show that, in the $\beta \rightarrow \infty$ limit, the first term dominates. Keeping only this term, we find that $e_a(\beta \rightarrow \infty) = \mathcal{E}_{\alpha_a}$. The same expression can be used to estimate the rate of convergence, which is exponential, with corrections of the form $e^{-\beta \Delta_a}$, where the energy scale Δ_a is determined by the details of the second term in Eq. (21). This rate can be as slow

as $\Delta_a = \mathcal{E}_{\alpha_{a+1}} - \mathcal{E}_{\alpha_a}$ or as fast as $\Delta_a = \mathcal{E}_\gamma - \mathcal{E}_{\alpha_a}$, where $\mathcal{E}_\gamma > \mathcal{E}_{\alpha_{d_{\text{proj}}}}$.

An ideal projection subspace would be one constructed using the exact eigenstates of H . In that case, the second term in Eq. (21) vanishes, and the thermal energies satisfy $e_{\alpha_i}(\beta) = \mathcal{E}_{\alpha_i}$ even for arbitrarily small β , as discussed previously. This was used recently to compute Fermi energies of free fermions using a Monte Carlo that typically suffers from a severe sign problem [14]. The next best scenario arises when perturbation theory provides a good approximation and the projection subspace of the free theory is used. In this situation, we obtain the best-case convergence with $\Delta_a = \mathcal{E}_\gamma - \mathcal{E}_{\alpha_{d_{\text{proj}}}}$ [6], and our method provides a non-perturbative approach that takes into account higher order corrections easily. Symmetries can also assist in constructing an effective projection subspace, since imposing symmetry constraints automatically restricts the energy eigenstates that have overlap with the chosen subspace.

In practical calculations, additional challenges arise when extracting the projected thermal energies $e_{\alpha_i}(\beta)$. These difficulties arise because the matrix elements of Z/Z^b and \tilde{E}/Z^b generally become small as the system size L or the inverse temperature β increases. In particular, the matrix Z/Z^b may become non-invertible. Even when Z/Z^b remains invertible, it can contain very small eigenvalues that become negative due to Monte Carlo errors. This is unphysical and can make the projected thermal energies complex. We will refer to these instabilities which result from signal to noise issues, as manifestations of the “sign problem” inherent in the method. Thus, obtaining $e_a(\beta)$ with controlled uncertainties requires careful analysis.

In this work, we employ the following procedure to compute $e_a(\beta)$. We first evaluate the diagonal elements Z_{aa}/Z^b , which must be nonzero and positive with small relative errors. Failure to achieve this indicates the need for higher Monte Carlo statistics; if this is not feasible, the corresponding projection state $|\psi_a\rangle$ is removed from the analysis, thereby reducing the dimension of the projection subspace. After ensuring that all diagonal elements are well determined, we compute the eigenvalues of the matrix Z/Z^b . These eigenvalues must again be positive and nonzero within small relative errors. If this condition is not met, it implies that the Monte Carlo method is encountering a signal to noise issue, akin to the sign problem. In this situation, high-energy states above some energy threshold are thermally suppressed, and the Monte Carlo sampling becomes insensitive to their presence. However, without these high-energy states, there may no longer exist d_{proj} independent projected vectors $|p_{\alpha_i}\rangle$ introduced earlier. In other words, the projected low-energy spectrum then contains fewer than d_{proj} eigenvalues. Consequently, not all d_{proj} projected effective thermal energies $e_a(\beta)$ remain meaningful. This issue manifests itself through vanishing eigenvalues of Z . In such cases, we discard the eigenvectors of Z/Z^b whose eigenvalues are zero or negative within uncertainties and

project both Z/Z^b and E/Z^b onto the remaining eigenvector subspace of Z/Z^b . The projected effective thermal energies are then computed from these reduced matrices. Because of this procedure, we cannot always extract all d_{proj} projected effective thermal energies, but the subset of energies that can be determined in this way is numerically stable and reproducible within errors.

We end this section by discussing a special one-dimensional projection subspace that arises when the sign problem can be solved. In this case, there exists a state $|\psi_a\rangle$ whose diagonal matrix element satisfies $Z_{aa}/Z^b = 1$ for all values of L and β . The corresponding one-dimensional projection subspace, $\mathbb{P}_{(a)}$, spanned by $|\psi_a\rangle$, can then be used to compute the projected effective thermal energy as

$$e_a(\beta) = E_{aa}(\beta)/Z^b = E_{aa}(\beta)/Z_{aa}. \quad (22)$$

The associated projected low-energy level—namely, the lowest energy eigenvalue whose eigenstate has a nonzero overlap with $|\psi_a\rangle$ —can then be determined with high accuracy by evaluating $e_a(\beta)$ at successively larger values of β , since the sign problem is absent. This idea is very similar to the projector Monte Carlo techniques discussed previously [28, 30].

In the above example, although the sign problem is absent for the one-dimensional projection subspace constructed from $|\psi_a\rangle$, it is likely to reappear once the subspace is enlarged by adding additional states $|\psi_c\rangle$. This is because the matrix Z/Z^b may develop small eigenvalues as β increases, which can be difficult to compute accurately using Monte Carlo methods.

V. THE TRANSVERSE FIELD ISING MODEL

As a first application of our method, we extract the lowest four energy levels at zero momentum, \mathcal{E}_0 , \mathcal{E}_1 , \mathcal{E}_2 , and \mathcal{E}_3 , of the TFIM at criticality in the presence of a small longitudinal field h . Zamolodchikov conjectured that the magnetic perturbation drives the critical Ising model towards an E_8 massive quantum field theory in the infrared (IR), which contains eight stable particles with precisely predicted mass ratios. Below the two particle continua, there are three masses $m_i = \mathcal{E}_i - \mathcal{E}_0$ from which we can create two universal ratios,

$$\frac{m_2}{m_1} = 2 \cos(\pi/5) \approx 1.618, \quad (23)$$

$$\frac{m_3}{m_1} = 2 \cos(\pi/30) \approx 1.989, \quad (24)$$

In the lattice theory, this prediction holds only in the scaling limit, where the lattice size L is large and the magnetic perturbation h is small, and the thermal perturbation is zero (tuned by the transverse field). Our goal here is to demonstrate that the PDMS method can be used to confirm Eq. (24). To the best of our knowledge, previous Monte Carlo attempts to extract this ratio were not successful [31], although it has been confirmed by other numerical and analytic approaches [32–37]. For recent

A. The Hamiltonian

The Hamiltonian of the TFIM at criticality in the presence of a longitudinal magnetic field h is given by

$$H = - \sum_{i=0}^{L-1} \left(\sigma_i^z \sigma_{i+1}^z + \sigma_i^x + h \sigma_i^z \right), \quad (25)$$

where i labels the sites on a periodic chain of length L , and σ_i^α are Pauli matrices that act on the two-dimensional Hilbert space of the i^{th} site.

We construct the continuous-time path integral, as discussed in Section II, using the basis states $|+\rangle$ and $|-\rangle$, which are eigenstates of the σ_i^x operator on each lattice site with eigenvalues $+1$ and -1 , respectively. We refer to these as the X -basis. For this purpose, we express H in the form described in Eq. (3) and identify

$$H_\ell = \left(- \sigma_i^z \sigma_{i+1}^z - \frac{h}{2} (\sigma_i^z + \sigma_{i+1}^z) - \frac{1}{2} [(1 + \sigma_i^x) + (1 + \sigma_{i+1}^x)] \right), \quad (26)$$

and $E_0 = L$, which makes all diagonal matrix elements in the X -basis negative semi-definite.

Each H_ℓ is a nearest-neighbor bond operator that connects sites i and $i + 1$ such that all matrix elements of $(-\varepsilon H_\ell)$ in the X -basis are positive. The link updates and spin updates, as discussed in Section IV are straightforward. When $h \neq 0$, the Ising symmetry is broken, but spin updates can still be constructed as explained in [38].

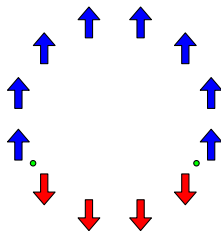


FIG. 3. A 2-domain wall state of length $\ell = 4$ for a chain of length $L = 12$. States like these make up our projection subspace.

B. Projection Subspace

We now discuss the choice of the projection subspace \mathbb{P} used to compute the lowest four eigenvalues of H at zero momentum for various values of h and L . Because the longitudinal field breaks the \mathbb{Z}_2 symmetry, momentum is the only remaining lattice symmetry that can be used to guide the construction of \mathbb{P} . The emergent E_8 masses are therefore purely dynamical.

Since our path integral is formulated in the X -basis, simple states in this basis generally have exponentially small overlap with the low-energy states. In contrast,

projection states chosen in the Z -basis—whose elements are eigenstates of σ_i^z —can have a much larger overlap. For example, consider the projection state

$$|\psi_1\rangle = 2^{-L/2} |\uparrow\uparrow\uparrow \dots \uparrow\rangle. \quad (27)$$

Using the relations $|\uparrow\rangle = (|+\rangle + |-\rangle)/\sqrt{2}$ and $|\downarrow\rangle = (|+\rangle - |-\rangle)/\sqrt{2}$, one can verify that $Z_{11}/Z^b = 1$, independent of L and β . As discussed at the end of Section IV, this implies that the sign problem is absent for this particular one-dimensional projection subspace.

Using exact diagonalization studies on the $L = 12$ lattice, as described in Appendix B 2, we added additional states to the projection subspace. One of these is the \mathbb{Z}_2 -flipped partner of Eq. (27), given by

$$|\psi_2\rangle = 2^{-L/2} |\downarrow\downarrow\downarrow \dots \downarrow\rangle. \quad (28)$$

While this state seems to have a good overlap with third excited state on small lattices, it causes instabilities on larger lattices. We drop it in our analysis for $L \geq 64$. We also found that states in which a contiguous block of ℓ neighboring spins is flipped have a strong overlap with the low-energy eigenstates. States of this form can be viewed as two-domain-wall configurations, as illustrated in Fig. 3. Translating these states and summing over all translations projects them onto the zero-momentum sector. We enumerate them as

$$|\psi_{\ell+2}\rangle = \frac{2^{-L/2}}{\sqrt{L}} \sum_{r=1}^L T^r |\underbrace{\downarrow\downarrow \dots \downarrow}_\ell \uparrow\uparrow \dots \uparrow\rangle, \quad (29)$$

where $\ell = 1, 2, \dots, L/2$. Here, T denotes the translation operator that shifts all spins by one lattice site to the right, and the summation enforces projection to zero momentum. In this work, we restrict $\ell \leq L/2$, although higher values ($L/2 < \ell < L$) could in principle be used. Thus, the total dimension of the projection subspace employed here is $d_{\text{proj}} = L/2 + 2$.

C. Projected Thermal Energies

We have used the PDMS method to compute the lowest four masses for various lattice sizes L , inverse temperatures β , and longitudinal field values h . While the full projection subspace \mathbb{P} is used to extract these quantities, care must be taken in removing zero modes in the Z/Z^b matrix, as discussed in Section IV. Additional details of this analysis are provided in Appendix B 2.

To confirm the reliability of the method, we first verified that it reproduces exact diagonalization results. In Fig. 4, we compare Monte Carlo data with exact diagonalization results for $L = 12$ at two values of h . The Monte Carlo data accurately reproduce the exact results for the first three energy levels. However, the fourth level, $e_3(\beta)$, begins to exhibit larger error bars around $\beta \approx 3$. We attribute this behavior to the fact that this level corresponds to a massive particle with $m_3 \approx 1.989 m_1$ (see

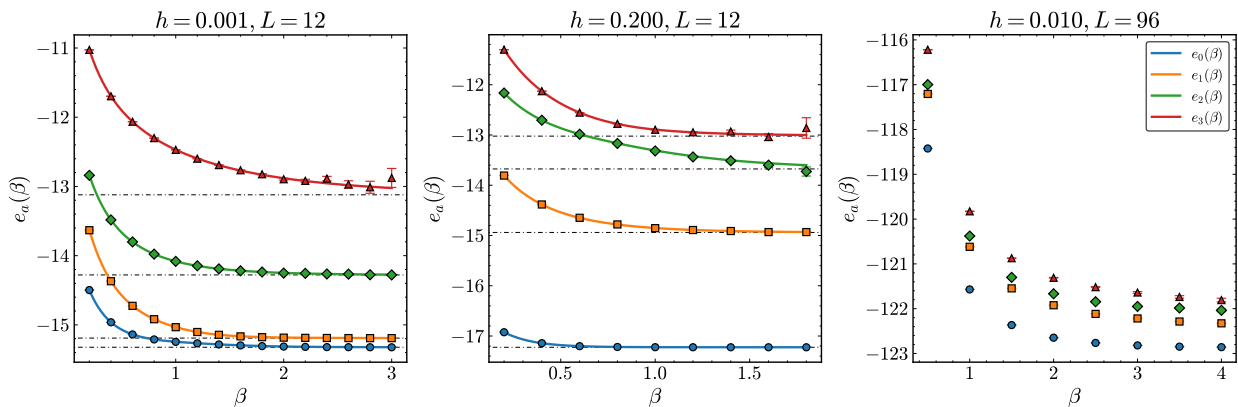


FIG. 4. The lowest four projected effective thermal energies obtained using the PDMS method for ($L = 12, h = 0.001$) (left), ($L = 12, h = 0.2$) (center), and ($L = 96, h = 0.01$) (right). The solid lines passing through the Monte Carlo data in the left and center panels represent exact diagonalization results. The dashed lines in these panels indicate the projected low-energy spectrum to which $e_a(\beta)$ is expected to converge in the $\beta \rightarrow \infty$ limit. The fourth level in the left and center panels begins to exhibit larger errors around $\beta \approx 3$, which we attribute to its proximity to the two-particle threshold, as discussed in the text. The right panel shows that the convergence of the energy levels is relatively slow due to the small gaps in the energy spectrum. Because the energies are extensive quantities, they scale with L , whereas the energy gaps do not. Consequently, obtaining accurate estimates of the gaps requires high statistics.

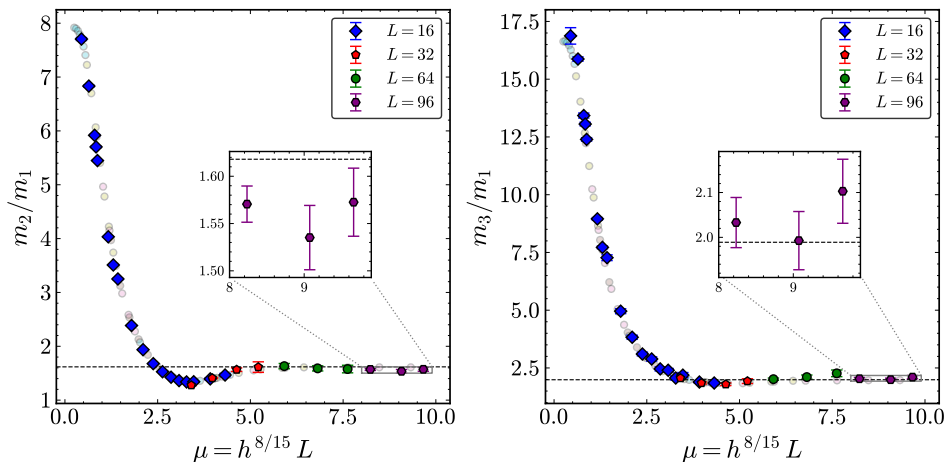


FIG. 5. Monte Carlo estimate of the mass ratio m_2/m_1 (left) and m_3/m_1 (right) as a function of μ . The dashed horizontal line shows the expected E_8 QFT result of $m_2/m_1 = 1.618$ and $m_3/m_1 = 1.989$. The inset shows our estimate at some of the largest values of μ we have computed. The light dots give estimates from exact diagonalization results at various small values of L and h .

Eq. (24)), which lies close to the two-particle threshold at $2m_1$. Consequently, it receives contributions from several two- m_1 particle states that naturally appear at energies above $2m_1$. This makes it difficult to extract m_3 reliably, beyond noting that its value is close to $2m_1$.

After confirming that the PDMS method accurately reproduces the lowest four energy levels at $L = 12$, we extended our calculations to a range of lattice sizes L , temperatures β , and longitudinal fields h to test the prediction of Eq. (24). The resulting values are summarized in Table II. We note that the raw energy levels can be computed reasonably accurately, although the relative errors of thermal energy gaps $e_i(\beta) - e_0(\beta)$ deteriorate as the energies increase.

D. Extraction of E_8 Mass Ratio

It is well known that the two-dimensional massive E_8 QFT emerges from a relevant magnetic perturbation of the Ising CFT. In the critical TFIM, introducing a small longitudinal field h generates a correlation length that scales as $\xi \sim h^{-8/15}$. If this CFT is probed on a finite lattice with L sites, a simple scaling hypothesis suggests that all observables in the theory become functions of a single dimensionless variable,

$$\mu = L h^{8/15}. \quad (30)$$

One immediate consequence is that the mass ratios m_i/m_1 should depend only on μ . In the limit $\mu = 0$, the system

L	β	h	$e_0(\beta)$	$e_1(\beta)$	$e_2(\beta)$	$e_3(\beta)$
16	2	0.071493	-21.2396(7)	-19.883(15)	-19.348(19)	-18.68(7)
		0.085771	-21.4240(9)	-19.913(14)	-19.21(4)	-18.63(11)
	2.5	0.002427	-20.40307(23)	-20.28470(25)	-19.5943(15)	-18.524(11)
		0.003640	-20.41362(21)	-20.27502(20)	-19.5933(17)	-18.553(15)
		0.003980	-20.41644(23)	-20.27194(27)	-19.5924(15)	-18.530(11)
		0.004320	-20.41960(26)	-20.26887(27)	-19.5983(16)	-18.551(11)
		0.007393	-20.45014(24)	-20.23879(21)	-19.5977(17)	-18.558(12)
		0.009085	-20.46848(21)	-20.22112(24)	-19.6002(15)	-18.559(15)
	3	0.010778	-20.48825(24)	-20.2173(4)	-19.6076(28)	-18.518(34)
		0.016556	-20.55444(18)	-20.1596(6)	-19.6125(26)	-18.60(4)
		0.022333	-20.62319(20)	-20.1021(8)	-19.6143(28)	-18.63(5)
		0.028111	-20.69247(22)	-20.0492(9)	-19.6134(25)	-18.70(5)
		0.033889	-20.76298(19)	-20.0042(16)	-19.6039(30)	-18.57(7)
		0.039667	-20.83495(20)	-19.9668(20)	-19.597(4)	-18.70(8)
		0.045444	-20.90689(15)	-19.930(4)	-19.5755(35)	-18.56(7)
		0.051222	-20.97981(15)	-19.913(4)	-19.553(4)	-18.78(9)
0.057000	-21.05325(20)	-19.906(5)	-19.514(6)	-18.54(13)		
3.5	0.001213	-20.40623(23)	-20.30395(15)	-19.6180(21)	-18.68(4)	
32	4	0.015000	-41.0715(4)	-40.4724(31)	-40.3061(17)	-39.836(16)
		0.020000	-41.18964(33)	-40.495(4)	-40.210(4)	-39.905(30)
		0.026650	-41.3490(4)	-40.549(10)	-40.096(22)	-39.91(5)
		0.033300	-41.5117(4)	-40.610(9)	-40.06(9)	-39.77(9)
64	3.5	0.011500	-82.0233(21)	-81.451(9)	-81.059(18)	-80.862(22)
		0.015000	-82.1653(20)	-81.518(11)	-81.121(27)	-80.69(8)
		0.018500	-82.3128(16)	-81.615(14)	-81.17(4)	-80.05(28)
96	4.5	0.010000	-122.8625(8)	-122.339(4)	-122.040(10)	-121.798(27)
		0.012000	-123.0026(8)	-122.434(6)	-122.130(18)	-121.870(35)
		0.013500	-123.1048(7)	-122.494(6)	-122.144(21)	-121.82(4)

TABLE I. Parameters (h, L, β) used to obtain the mass ratio m_2/m_1 as a function of μ displayed in Fig. 5. At these parameters we can use the PDMS method to reliably extract the mass ratio for $\mu \in [0.446, 9.663]$ which covers both the Ising CFT and the E_8 QFT.

L	β -range	h_{\parallel} -range	μ -range
16	2.0-3.0	0.001-0.0858	0.446-4.318
32	4.0	0.015-0.033	3.407-5.213
64	3.5	0.012-0.019	5.194-7.621
96	4.0	0.01-0.0135	8.234-9.663

TABLE II. Parameters $(h_{\parallel}, L, \beta)$ used to obtain the mass ratio r_1 as a function of μ displayed in Fig. 5. These parameters were chosen for computational tractability of the PDMS method.

approaches the Ising CFT, where, for example, $m_2/m_1 = 8$. In the opposite limit $\mu \rightarrow \infty$, the theory begins to describe the E_8 QFT, where $m_2/m_1 = 1.618$.

In a lattice calculation, any finite value of L introduces corrections that break conformal invariance, so the above statements hold strictly only in the simultaneous limits $h \rightarrow 0$ and $L \rightarrow \infty$, with μ held fixed. In practice, however, the scaling hypothesis is already observed to work well even for moderate system sizes. For example, as shown in Fig. 4, when $h = 0.001$ (corresponding to

$\mu = 0.301$), we obtain $m_2/m_1 = 7.888(37)$, close to the Ising CFT prediction of 8. Conversely, when $h = 0.2$ (corresponding to $\mu = 5.086$), we find $m_2/m_1 = 1.526(40)$, consistent with the E_8 QFT prediction of 1.618.

To compute the mass ratios in the E_8 QFT, we must focus on the limit $\mu \rightarrow \infty$ with $h \rightarrow 0$ and $L \rightarrow \infty$. Reaching this regime numerically requires identifying a set of parameters (h, L, β) for which the projected thermal energies $e_a(\beta)$ have converged to the projected low-energy spectrum within small statistical errors.

The main difficulty at large L with fixed μ is that the energy gaps decrease while each individual energy scales with L . Consequently, accurately determining the gaps requires substantial statistics, and larger values of β are needed for convergence. This challenge is compounded by the fact that the physical Hilbert space grows exponentially with L , whereas the projection subspace grows only linearly, leading to a reduced overlap between any energy eigenstate of H and the projection subspace.

Conversely, using smaller L and larger h increases the energy gaps. However, in this regime, the matrix Z/Z^b

can become nearly singular at large β , since some of its eigenvalues scale as $e^{-\beta m_i}$ and may vanish within Monte Carlo errors. This is effectively a manifestation of the sign problem, which renders Z/Z^b non-invertible.

Despite these challenges, we have identified a regime of parameters where it is still possible to reliably extract the ratio m_2/m_1 . The corresponding parameter ranges are listed in Table I, and the results for the lowest four projected thermal energies in this regime are summarized in Table II.

Our final results for the ratios m_2/m_1 and m_3/m_1 as functions of $\mu = Lh^{8/15}$, obtained from the PDMS, are shown in Fig. 5. We find that the ratios saturate to the expected E_8 value for $\mu \gtrsim 6$, within expected errors. We have verified that our results are consistent with the known universal scaling curve for these ratios as a function of μ [32].

VI. THE SHASTRY–SUTHERLAND MODEL

As a second application, in this section, we investigate whether the PDMS method can be applied to study the highly frustrated Shastry–Sutherland model (SSM) at various coupling strengths. Since the model is known to suffer from a severe sign problem, our first goal here is modest: we aim to reproduce the values of the projected thermal energies $e_a(\beta)$ for small lattice sizes and small β , which can also be computed using exact diagonalization. These results can be found in Sections VID and VIE.

Our second goal is to demonstrate that our method readily extends to larger lattices beyond the reach of exact diagonalization methods, as long as β is kept small. We further argue that even relatively small values of β can sometimes yield results that are close to the zero-temperature limit, provided a suitable projection subspace is chosen. To this end, we focus on two different regimes of the SSM on an $L = 8$ lattice, where we can compare results from our method with those obtained from other reliable approaches in earlier work. In Section VIF, we show that we can accurately compute the lowest three energy levels of the two-dimensional Heisenberg model on the square lattice (the unfrustrated limit of the SSM) using data at small values of β . In Section VIG, we examine the first excited energy level of the SSM at ($J = 1.0, J' = 0.5$), which is accessible in perturbation theory. We find that the energy gap between this level and the ground state at $L = 4$ is already in excellent agreement with perturbation theory, suggesting that larger lattice sizes are unnecessary. This conclusion is supported by our calculations at $L = 8$, which yield results consistent within statistical errors with those obtained at $L = 4$. Calculations at $L = 8$ are noisier, and reaching larger values of β becomes increasingly challenging.

In all these studies of the SSM model, we consider two simple projection subspaces that distinguish between two symmetry sectors of the model and examine the challenges involved in extracting the projected low-energy spectrum

associated with these subspaces.

A. The Hamiltonian

The Hamiltonian of the SSM is given by

$$H = J' \sum_{\langle ij \rangle} \mathbf{s}_i \cdot \mathbf{s}_j + J \sum_{\langle\langle ij \rangle\rangle} \mathbf{s}_i \cdot \mathbf{s}_j, \quad (31)$$

where i, j label sites on an $L \times L$ periodic square lattice. The quantum spin- $\frac{1}{2}$ operators $\mathbf{s}_i = (s_i^x, s_i^y, s_i^z)$ associated with site i interact antiferromagnetically with operators \mathbf{s}_j on neighboring sites j through two types of bonds, denoted by $\langle ij \rangle$ for the nearest-neighbor bonds and $\langle\langle ij \rangle\rangle$ for a specific set of diagonal bonds. An illustration of these bonds on a 4×4 periodic lattice is shown in Fig. 6. Further details of our convention for labeling the lattice and the bonds can be found in Appendix C.

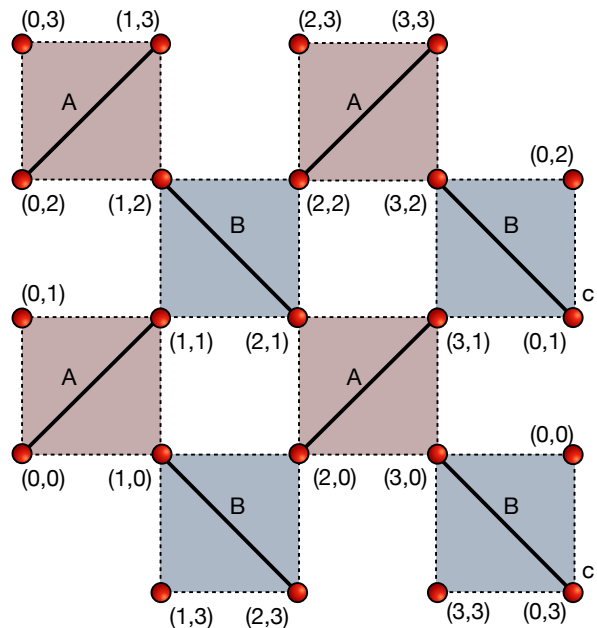


FIG. 6. Illustration of the Shastry–Sutherland lattice on a 4×4 periodic system. Thin dashed black lines indicate the $\langle ij \rangle$ bonds with interaction weight J' bonds, while thick solid lines represent the $\langle\langle ij \rangle\rangle$ bonds with interaction weight J . The coordinates of each site are also shown for convenience.

We argued in Section II that it is important to rewrite H in the form

$$H = \sum_{\ell} H_{\ell} + E_0, \quad (32)$$

to construct the path integral. For the SSM, ℓ refers to interactions on both $\langle ij \rangle$ and $\langle\langle ij \rangle\rangle$ bonds. We define

$$H_{\ell} = J_{ij} (\mathbf{s}_i \cdot \mathbf{s}_j - \frac{1}{4}), \quad (33)$$

where J_{ij} equals either J or J' , depending on whether (i, j) corresponds to an $\langle ij \rangle$ or $\langle\langle ij \rangle\rangle$ bond, respectively. It is straightforward to verify that

$$E_0 = \sum_{i,j} J_{ij} = \left(\frac{J'}{2} + \frac{J}{8} \right) L^2, \quad (34)$$

where E_0 is chosen such that all diagonal matrix elements of H_ℓ are either zero or negative in the chosen basis.

Using Eq. (33), we can construct the path integral and design a Monte Carlo algorithm as discussed in Sections II and III. We employ the conventional s_i^z eigenbasis, labeled by $|\uparrow\rangle$ and $|\downarrow\rangle$, although other types of dimer bases could be more effective in mitigating sign problems [39]. To partially alleviate the sign problem in the s_i^z basis, we work in the spin-cluster representation and include the entropy factor that arises from summing over an entire class of spin configurations during the bond updates. This helps in reducing the fluctuations while computing the Z and E matrices using Eqs. (17) and (18).

B. Projection Subspaces

Symmetries often provide valuable guidance in constructing suitable projection subspaces. Since the SSM is invariant under spin rotations, it is useful to define projection subspaces that isolate a single spin sector s with a specific magnetic quantum number m . However, in this work, we consider a simpler conserved quantity associated with the operator

$$\hat{Q} = \prod_i (2s_i^x), \quad (35)$$

whose eigenvalues are ± 1 . Because $[H, \hat{Q}] = 0$, all energy eigenstates can be classified according to their \hat{Q} quantum number. Based on \hat{Q} , we define two projection subspaces, \mathbb{P}_+ and \mathbb{P}_- , which distinguish energy eigenstates with eigenvalues $Q = +1$ and $Q = -1$, respectively. These subspaces are constructed as direct-product states of single-site and two-site (dimer) basis states. Details of how these local states are defined are provided in Appendix C.

Our \mathbb{P}_+ subspace is four-dimensional and constructed as the span of four simple projection states defined as

$$\begin{aligned} |\psi_1\rangle &= \bigotimes_{i \in \text{even}} (|\uparrow\rangle + |\downarrow\rangle)_i \bigotimes_{j \in \text{odd}} (|\downarrow\rangle - |\uparrow\rangle)_j, \\ |\psi_2\rangle &= \bigotimes_{\langle\langle ij \rangle\rangle} |\psi_t\rangle_{\langle\langle ij \rangle\rangle}, \\ |\psi_3\rangle &= \bigotimes_{\substack{\langle ij \rangle \\ x_i \text{ even}, x_j = x_i + 1 \\ x_i \text{ odd}, x_j = x_i - 1}} |\psi_s\rangle_{\langle ij \rangle}, \\ |\psi_4\rangle &= \bigotimes_{\substack{\langle ij \rangle \\ x_i \text{ even}, x_j = x_i + 1 \\ x_i \text{ odd}, x_j = x_i - 1}} |\psi_t\rangle_{\langle ij \rangle}, \end{aligned} \quad (36)$$

where the dimer product states $|\psi_s\rangle$ and $|\psi_t\rangle$ are defined in Eqs. (C1) and (C2). These states are illustrated for $L = 2$ in Fig. 12 and for $L = 4$ in Fig. 13. It is straightforward to verify that all of these states are eigenstates of the \hat{Q} operator with eigenvalue $+1$.

It is also straightforward to verify that another $Q = +1$ state, constructed as the product of singlet dimers on the $\langle\langle ij \rangle\rangle$ bonds,

$$|\psi_0\rangle = \bigotimes_{\langle\langle ij \rangle\rangle, x_i \text{ even}} |\psi_s\rangle_{\langle\langle ij \rangle\rangle}, \quad (37)$$

is an eigenstate of H with eigenvalue

$$\mathcal{E}_S = -\frac{3}{8} J L^2, \quad (38)$$

for all values of (J, J') . One of the central results of Ref. [26] is that, for $J' \leq J/2$, $|\psi_0\rangle$ is also the ground state of H .

When $J' = 0$, since the $\langle\langle ij \rangle\rangle$ dimers do not interact, all the excited states can be constructed exactly. The first excited state, which has an energy gap of order J , can be obtained by placing all $\langle\langle ij \rangle\rangle$ dimers in the spin-singlet state except for one, which is placed in the triplet state $|\psi_t\rangle$ defined in Eq. (C2). The state in which the triplet is connected to the origin $(x_i, y_i) = (0, 0)$ is given by

$$|\phi_1\rangle = |\psi_t\rangle_{\substack{\langle\langle ij \rangle\rangle \\ x_i \text{ even}}} \bigotimes_{\langle\langle ij \rangle\rangle' \neq \langle\langle ij \rangle\rangle} |\psi_s\rangle_{\langle\langle ij \rangle\rangle'}. \quad (39)$$

The other states in the subspace, $|\phi_a\rangle$ ($a = 2, 3, \dots, L^2/2$), are obtained by translating the triplet to other $\langle\langle ij \rangle\rangle$ bonds. Based on our discussion in Section IV, an ideal projection subspace for studying the excited spectrum in the perturbative regime of small J' would be this $L^2/2$ -dimensional degenerate subspace of first excited states at $J' = 0$. This subspace naturally has $Q = -1$, as can be verified, and forms our \mathbb{P}_- subspace. The various states in this subspace for $L = 2$ and $L = 4$ are pictorially illustrated in the appendix in Figs. 12 and 13.

For small J' , the states in \mathbb{P}_- mix only at high order in perturbation theory. This suggests that $\langle \phi_a | e^{-\beta H} | \phi_b \rangle \propto \delta_{ab}$ would be a good approximation, at least for small values of J' . Interestingly, we find that this behavior persists even at larger values of J' , partly due to lattice symmetries and partly due to dynamical effects. While at small J' the \mathbb{P}_- subspace has a large overlap with the first excited state, at larger values of J' it mixes only weakly with lower-energy states, indicating that it is an optimal subspace for exploring the projected low-energy spectrum only for small values of J'/J .

C. Choice of Couplings

We focus on four values of the couplings (J, J') , motivated by the physics of the SSM, and compute the projected thermal energies for small lattice sizes L and

Coupling	Projected Low Energy Spectrum	
	\mathbb{P}_+	\mathbb{P}_-
	$\mathcal{E}_1, \mathcal{E}_2, \mathcal{E}_3, \mathcal{E}_4$	$\mathcal{E}_1 = \mathcal{E}_2$
$(J = 0, J' = 1)$	E_1, E_2, E_3, E_5	$E_4(2)$
$(J = 1, J' = 0.5)$	E_1, E_1, E_2, E_3	$E_2(2)$
$(J = 1, J' = 0.66)$	E_1, E_2, E_3, E_5	$E_4(2)$
$(J = 1, J' = 0.75)$	E_1, E_2, E_3, E_5	$E_4(2)$

TABLE III. Projected low energy spectrum at various couplings at $L = 2$. The energies E_a are listed in Table VIII. In the \mathbb{P}_- subspace the two energies are degenerate. The levels in the projected low energy spectrum are shown as dashed lines in Fig. 7.

inverse temperatures β . The goal is to explore the challenges involved in extracting the projected low-energy spectrum associated with \mathbb{P}_+ and \mathbb{P}_- .

Among the four couplings, the first case we study is $(J = 0, J' = 1)$, where the SSM reduces to the 2D-unfrustrated Heisenberg quantum antiferromagnet. Here, the low-energy physics is that of a spontaneously broken continuous symmetry with a dense spectrum of low-lying excitations. Our goal in this case is to examine how well the \mathbb{P}_+ subspace reproduces the low-energy spectrum. The second coupling we consider is $(J = 1, J' = 0.5)$, where the SSM lies in a gapped phase. Here, our main objective is to determine whether the energy gap can be extracted using the \mathbb{P}_- subspace. We then investigate the couplings $(J = 1, J' = 0.66)$ and $(J = 0, J' = 0.75)$, which lie close to two phase transitions predicted in the SSM [27] using both the projection subspaces to learn how they perform.

D. Results at $L = 2$

In this section, we present our results for the projected thermal energies $e_a(\beta)$ at $L = 2$ for both projection subspaces and examine how they converge to the projected low-energy spectrum. To identify this spectrum, it is first useful to distinguish the distinct energy levels of H . We denote these as E_a ($a = 1, 2, \dots$), ordered such that $E_1 \leq E_2 \leq E_3 \leq \dots$. Each level is characterized by its spin representation s and a degeneracy factor g arising from exact lattice symmetries. The total degeneracy of level E_a is therefore $g(2s + 1)$. If different spin representations exhibit additional accidental degeneracies, the corresponding energies are treated as distinct levels. Using these energies, together with information about the overlap of the associated energy eigenstates with the projection subspace, we can identify the projected low-energy spectrum $\mathcal{E}_1, \mathcal{E}_2, \dots$, discussed in Section IV. This allows us to study the convergence of $e_a(\beta)$ to \mathcal{E}_a .

For $L = 2$, all eigenstates of H can be constructed as

Coupling	Projected Low Energy Spectrum	
	\mathbb{P}_+	\mathbb{P}_-
	$\mathcal{E}_1, \mathcal{E}_2, \mathcal{E}_3, \mathcal{E}_4$	$\mathcal{E}_1 = \dots = \mathcal{E}_4,$ $\mathcal{E}_5 = \dots = \mathcal{E}_8$
$(J = 0, J' = 1)$	E_1, E_2, E_3, E_7	$E_4(4), E_5(4)$
$(J = 1, J' = 0.5)$	E_1, E_4, E_6, E_{32}	$E_2(4), E_3(4)$
$(J = 1, J' = 0.66)$	E_1, E_2, E_3, E_9	$E_5(4), E_7(4)$
$(J = 1, J' = 0.75)$	E_1, E_2, E_3, E_8	$E_5(4), E_6(4)$

TABLE IV. Projected Low Energy Spectrum at various couplings at $L = 4$. The energies E_a are listed Table IX. In the \mathbb{P}_- subspace the eight energies split into two distinct levels each of which contains four degenerate states. The levels in the projected low energy spectrum are shown as dashed lines in Fig. 8.

direct products of states on the two diagonal bonds, as discussed in Appendix C. The distinct ordered energies E_a for the four chosen couplings are summarized in Table VIII. Using the relations provided in Appendix C and following the procedure outlined in Section IV, we can identify the projected low-energy spectrum in the two different subspaces. These results are shown in Table III. Note that since the dimension of the \mathbb{P}_+ subspace is four, we identify four energies. Some of these energies are accidentally degenerate at certain couplings. However, although the dimension of the \mathbb{P}_- subspace is two, we display only one energy because both are identical due to lattice symmetry as explained in Section VI B.

A comparison between the projected thermal energies obtained from our Monte Carlo data and the exact results at all couplings is shown in Fig. 7. As the figure illustrates, these energies converge exponentially to the projected low-energy spectrum, as expected, even at small values of β . Hence, it seems the chosen projection subspaces are nearly ideal. We obtain all five distinct energy eigenvalues with high accuracy even at $\beta = 1.0$.

E. Results at $L = 4$

We now repeat the above analysis for $L = 4$. In this case, we use exact diagonalization to compute the eigenvalues and eigenvectors of H . In Table IX, we list the lowest 45 distinct energy levels E_a , along with their spin quantum numbers s and representation degeneracies g , for the four coupling sets considered. From this table, we observe that the dimer state of Eq. (37), with energy $\mathcal{E}_5 = -6$, is the ground state at both $(J = 1, J' = 0.5)$ and $(J = 1, J' = 0.66)$. However, it becomes the $a = 10$ level at $(J = 1, J' = 0.75)$ and no longer appears among the lowest 45 distinct levels when $(J = 0, J' = 1)$.

The first and second excited states also evolve with

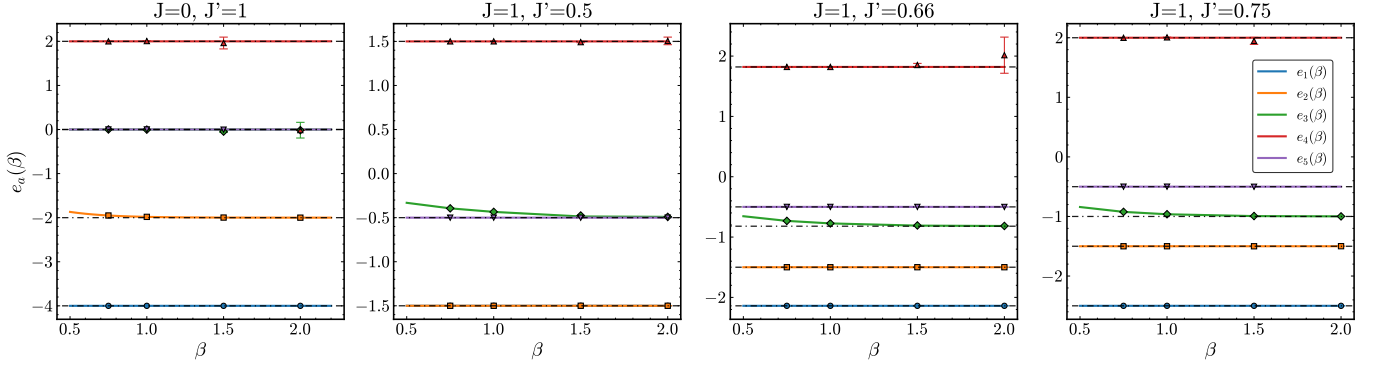


FIG. 7. The projected thermal energies extracted using the two projection subspaces \mathbb{P}_+ and \mathbb{P}_- discussed for $L = 2$. The two distinct energies in the \mathbb{P}_- subspace are degenerate and hence only one is shown. The Monte Carlo data was obtained only at $\beta = 0.75, 1, 1.5, 2$. The solid lines are exact diagonalization results. The projected low energy spectrum is shown as horizontal dashed lines and their quantitative values can be found in Table III. While in general there are five distinct projected low energy levels, at $(J = 0, J' = 1)$ and $(J = 1, J' = 0.5)$ some levels become degenerate as can be seen from Table III.

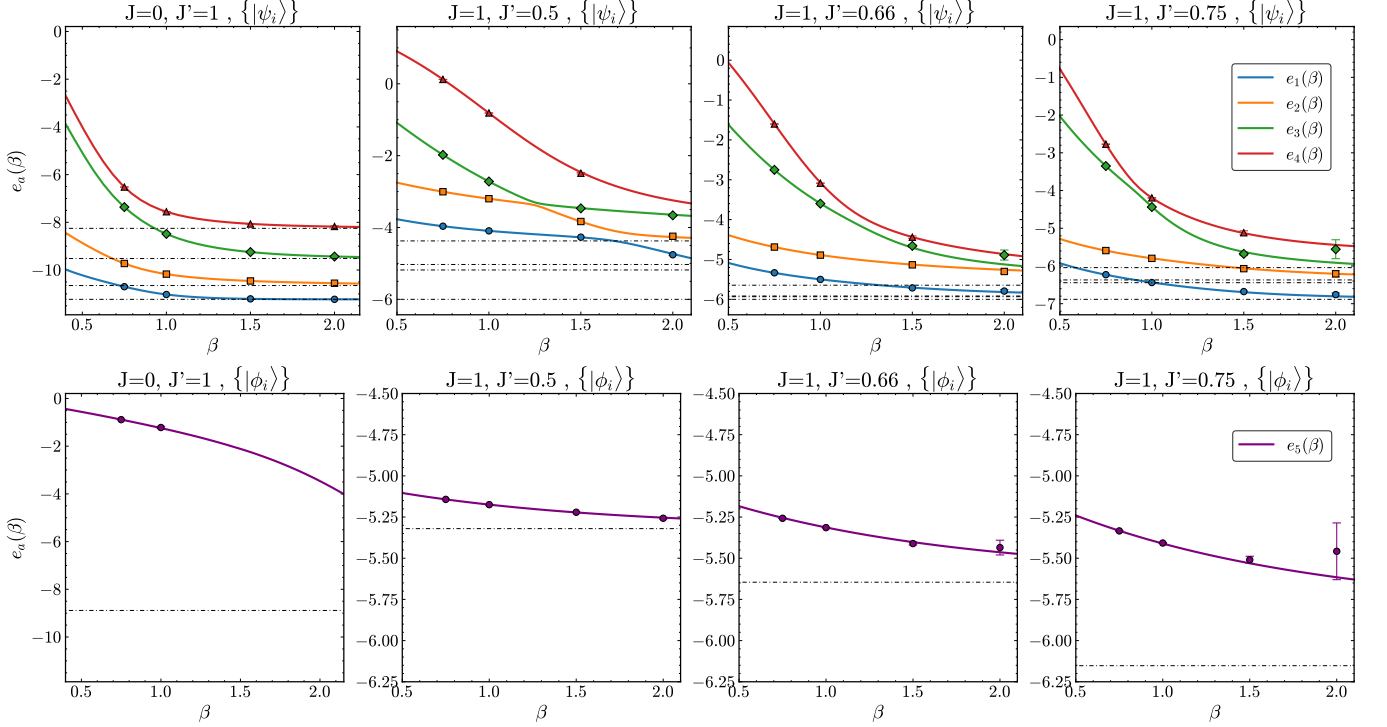


FIG. 8. Projected thermal energies $e_a(\beta)$ extracted using \mathbb{P}_+ (top row) and \mathbb{P}_- (bottom row) for $L = 4$. While \mathbb{P}_- is eight-dimensional, the energies split into two four-dimensional degenerate subspaces with two distinct but nearly equal values. Hence, we show only one representative degenerate energy for the entire subspace. The Monte Carlo data were obtained at $\beta = 0.75, 1.0, 1.5, 2.0$. The solid lines represent exact diagonalization results, which consistently agree with the Monte Carlo data, demonstrating the validity of our PDMS method. The projected low-energy spectrum is shown as horizontal dashed lines in each panel, and their numerical values can be found in Table IV. Missing data indicate the presence of a sign problem and the necessity to omit certain states during the analysis. The numerical values of the Monte Carlo data at $\beta = 2$ and the corresponding dashed-line energies are listed in Table V.

the couplings. For $(J = 1, J' = 0.5)$, these two states are nearly degenerate triplets with energies $E_1 \approx E_2 \approx -5.320$, each triplet being fourfold degenerate. These states overlap with the eight-dimensional \mathbb{P}_- subspace. The overlap information for some of the low-energy states

with $|\phi_1\rangle$ is shown in Table X. In fact, the overlaps with all eight projection states $|\phi_i\rangle$, $i = 1, \dots, 8$, are very similar, and hence only one of them is displayed. As argued earlier, the energy splitting among the states that overlap with \mathbb{P}_- is expected to be small at small J' , and this behavior is

Projection Subspace	$(J = 0, J' = 1)$		$(J = 1, J' = 0.5)$		$(J = 1, J' = 0.66)$		$(J = 1, J' = 0.75)$	
	Exact ($\beta \rightarrow \infty$)	Monte Carlo ($\beta = 2$)	Exact ($\beta \rightarrow \infty$)	Monte Carlo ($\beta = 2$)	Exact ($\beta \rightarrow \infty$)	Monte Carlo ($\beta = 2$)	Exact ($\beta \rightarrow \infty$)	Monte Carlo ($\beta = 2$)
\mathbb{P}_+	-11.22848...	-11.2269(2)	-6.00000...	-4.76(2)	-6.00000...	-5.83(4)	-6.88440....	-6.79(5)
	-10.64988...	-10.5524(2)	-5.18260...	-4.26(3)	-5.93309...	-5.33(6)	-6.44305...	-6.34(6)
	-9.51768...	-9.436(3)	-5.02962...	-3.68(4)	-5.91680...	-5.1(1)	-6.37022...	-5.9(3)
	-8.25282...	-8.17(2)	-4.37361...	-3.1(2)	-5.62894...	-4.7(2)	-6.04382...	-4.7(4)
\mathbb{P}_-	-8.79437...	-	-5.32028...		-5.64562...	-5.44(5)	-6.15238....	-5.5(2)

TABLE V. Comparison of the projected thermal energies $e_a(\beta)$ at $\beta = 2$ with the projected low-energy spectrum ($e_a(\beta = \infty)$) at various couplings for $L = 4$. The first four rows correspond to \mathbb{P}_+ , while the last row lists the degenerate level in the eight-dimensional \mathbb{P}_- subspace. The missing value indicates the presence of a sign problem.

indeed visible even at $J' = 0.5$. More accurately the eight degenerate first excited states at $J' = 0$, split into two distinct four-fold degenerate levels given by E_2 and E_3 at $J' = 0.5$. These then naturally form the projected low-energy spectrum of the \mathbb{P}_- subspace at $(J = 1, J' = 0.5)$. The energy gap between these states and the ground state is approximately 0.68. In contrast, using the overlap information in Table XI, we observe that the projected low-energy spectrum of the \mathbb{P}_+ subspace is E_1, E_4, E_6 , and E_{32} .

At $(J = 1, J' = 0.66)$, the lowest-energy excitations are no longer among the \mathbb{P}_- states. These triplets now correspond to E_5 and E_7 , each forming a four-dimensional subspace, with splittings that remain small. These states constitute the projected low-energy spectrum of \mathbb{P}_- . Several new $s = 0$ states appear below them. The first and second excited states are singlets separated by a very small gap of about 0.015, with the second excited state being doubly degenerate, most likely due to a lattice symmetry. The energy gap between the first excited state and the ground state is even smaller, roughly 0.07. Using Table XI, we find that the projected low-energy spectrum of \mathbb{P}_+ consists of E_1, E_2 , one of the E_3 states, and E_9 .

At $(J = 1, J' = 0.75)$, the ground state changes to a distinct singlet with energy around -6.88 . The first excited state is another singlet, doubly degenerate due to lattice symmetry, separated by a gap of approximately 0.44. The second excited state is a triplet lying about 0.07 above the first excited state. Using information from Table XI, we conclude that these four states (i.e., E_1, E_2, E_3 , and E_8) form the projected low-energy spectrum of the \mathbb{P}_+ subspace. From Table X, we observe that the states E_5 and E_6 , both fourfold degenerate, form the projected low-energy spectrum of the \mathbb{P}_- subspace. Again, the energy splitting among them remains small, though somewhat larger than for smaller values of J' .

Finally, for $(J = 0, J' = 1)$, the ground state is a singlet, followed by a triplet and a quintuplet as the first

and second excited states, respectively—consistent with expectations for an antiferromagnet. Using Table XI, we find that the projected low-energy spectrum of the \mathbb{P}_+ subspace is E_1, E_2, E_3 , and E_7 . From Table X, we see that the two fourfold-degenerate subspaces with energies E_4 and E_5 form the projected low-energy spectrum of the \mathbb{P}_- subspace. However, Table X also shows that the overlaps of these states—and even of some higher-energy states—are quite small. Hence, we do not expect the \mathbb{P}_- subspace to be a good choice at $(J = 0, J' = 1)$, and the corresponding projected thermal energies are expected to converge very slowly.

The discussion above regarding the projected low-energy spectrum of both \mathbb{P}_+ and \mathbb{P}_- subspaces at various couplings is summarized in Table IV. As discussed in Section IV, the rate at which the projected thermal energies converge to the projected low-energy spectrum depends on the second term in Eq. (21), which involves the states $|p_\gamma\rangle$ that capture the overlap of higher excited states with the projection subspaces. In a generic many-body quantum system, the energy spectrum becomes increasingly dense at higher energies—this is also the case for the SSM. As seen in Table X and Table XI, our projection subspaces have significant overlap with several higher-energy states. Thus, we do not expect them to provide an optimal basis in which the projected thermal energies $e_a(\beta)$ rapidly converge to the projected low-energy spectrum.

The convergence of the projected thermal energies is shown in Fig. 8. In these plots, the solid lines represent exact diagonalization results, while the data points with error bars correspond to our Monte Carlo estimates. In all cases, the Monte Carlo results agree with the exact values within statistical uncertainties, confirming the reliability of our PDMS method. The horizontal dashed lines indicate the projected low-energy spectrum (also listed in Table IV); these are the levels that the solid curves approach as $\beta \rightarrow \infty$, a trend we have verified with exact calculations. Although our two projection

subspaces are not optimal in general, they perform well in several cases. For instance, \mathbb{P}_+ helps us compute the first four levels of the projected low energy spectrum with reasonable accuracy at $(J = 0, J' = 1)$, while \mathbb{P}_- performs well in computing the first excited states at $(J = 1, J' = 0.5)$. For $(J = 1, J' = 0.66)$, the lowest level in the \mathbb{P}_+ projection subspace has converged to within about three percent, while the degenerate level in the \mathbb{P}_- subspace lies about five percent away and exhibits larger statistical errors. We see similar results for the case at $(J = 1, J' = 0.75)$; \mathbb{P}_+ allows us to compute the ground-state energy to within one percent whereas the \mathbb{P}_- subspace remains far from convergence. A quantitative comparison between the projected low-energy spectrum and $e_a(\beta)$ at $\beta = 2$ is presented in Table V.

It would be interesting to explore alternative projection subspaces guided by both spin and lattice symmetries. One manifestation of these symmetries appears in the allowed degeneracies g of the spin representations. For example, from Table IX, we observe that for $J = 1$, the degeneracies take the values $g = 1, 2, 4$, whereas for $J = 0$, they are $g = 1, 3, 4, 6, 8$. A more detailed understanding of these degeneracies, and the use of this information to design improved projection subspaces, could lead to more efficient and accurate implementations of our method.

F. The Quantum Heisenberg Limit

We now investigate the performance of our PDMS method on an $L = 8$ lattice, which lies beyond the reach of exact diagonalization studies. We first focus on the case $(J = 0, J' = 1)$, which turns the SSM into the well studied two dimensional quantum Heisenberg model. In this study we focus on the \mathbb{P}_+ subspace. In the quantum Heisenberg limit, we can show that $Z_{11}/Z^b = 1$ for all values of β and L , a result that can be easily proved, for example, using meron-cluster properties [24]. This implies that the sign problem is absent, at least for the projection state $|\psi_1\rangle$ at this coupling.

In this limit, our Monte Carlo method therefore enables a high-precision determination of $e_1(\beta)$ associated with the projection subspace $\mathbb{P}_{(1)}$ spanned by $|\psi_1\rangle$. At large values of β , this projected thermal energy is expected to yield the ground-state energy of the two-dimensional Heisenberg antiferromagnet. Results for the $L = 8$ lattice are shown in the second column of Table VI and also plotted in Fig. 9. We observe that $e_1(\beta)$ decreases gradually with increasing β . A previous study performed at $\beta = 64$ reported the ground-state energy to be $-43.103168(250)$ [40], whereas our current calculation yields, $e_1(\beta = 15) = -43.0724(3)$, which has clearly not converged to the low temperature limit.

Rather than taking the large- β limit with $\mathbb{P}_{(1)}$, we can instead use \mathbb{P}_+ to test whether increasing the dimension of the projection subspace improves the rate of convergence. The projected thermal energies obtained using \mathbb{P}_+ are listed in the right four columns of Table VI and also

plotted in Fig. 9. We now find $e_1(\beta = 3.0) = -43.11(6)$ and $e_1(\beta = 5.0) = -43.11(1)$, both showing clear signs of convergence to the ground state result of [40]. The fact that we can obtain the ground state energy with an error of less than 0.2% even at the value of $\beta = 3.0$ is impressive.

We note that the Monte Carlo errors in the calculation of $e_1(\beta)$ arise from contributions across the entire projection subspace. Sign problems can reemerge through other projection states for which Z_{aa}/Z^b becomes small as β increases. The use of larger projection subspaces therefore typically restricts us to smaller values of β . We show this behavior in Table VI. At $\beta = 3.0$, we are able to extract all four $e_a(\beta)$ values, but at $\beta = 5.0$ we had to discard the state $|\psi_4\rangle$ to obtain reliable results due to zero modes creeping in from that state. However, this reduction still allows us to recover the three lowest levels with equal or higher accuracy. Notably, $d_{\text{proj}} = 3$ performs better than $d_{\text{proj}} = 1$ for the ground-state calculation at $\beta = 5.0$. For $\beta = 10$ and 15, the projection subspace had to be reduced further. By retaining only $|\psi_1\rangle$ and $|\psi_2\rangle$, we obtained more accurate estimates for the ground-state energy, $-43.1036(3)$, and the first excited-state energy, $-42.927(1)$. This estimate of the ground-state energy is consistent with that obtained at $\beta = 5.0$ with $d_{\text{proj}} = 3$. Another earlier work (see [41]) reported the first excited energy as $-42.90(4)$, consistent with our result but with substantially larger errors. For the second excited state, the previous estimate of $-42.54(3)$ and our result of $-42.63(8)$ at $\beta = 3$ are also consistent, although our uncertainties are larger. We expect that a more carefully chosen projection subspace could improve the precision of some the higher excited states further.

G. Perturbative Energy Gap at small J'/J

In Section VIB we explained that \mathbb{P}_- is an optimal subspace for computing the first excited energy level for small values of J'/J . Here we verify this by exploring how the \mathbb{P}_- subspace performs at $(J = 1, J' = 0.5)$. The energy gap between the ground state (E_1) and the first excited state (E_2) was computed in perturbation theory to very high orders [42] and the first few terms of this series are given by

$$(E_2 - E_1) = 1 - \left(\frac{J'}{J}\right)^2 - \frac{1}{2}\left(\frac{J'}{J}\right)^3 - \frac{1}{8}\left(\frac{J'}{J}\right)^4 + \dots \quad (40)$$

In Fig. 10, we plot the perturbation theory result for the gap as a function of J'/J . For comparison we also show the results for the gap obtained using exact diagonalization on a $L = 4$ lattice. The Monte Carlo results presented in Fig. 8 for $L = 4$, $J'/J = 0.5$ at $\beta = 0.75$ and $\beta = 2$ are also shown. These results suggest that the energy gap saturates even at $L = 4$ and going to larger

β	Projected subspace $\mathbb{P}_{(1)}$	Projected subspace \mathbb{P}_+			
	$e_1(\beta)$	$e_1(\beta)$	$e_2(\beta)$	$e_3(\beta)$	$e_4(\beta)$
2.0	-42.6405(5)	-42.95(2)	-42.54(2)	-42.25(14)	-40.1(4)
3.0	-42.8159(2)	-43.11(6)	-42.75(6)	-42.60(8)	-40.8(8)
5.0	-42.9406(2)	-43.11(1)	-42.852(3)	-42.63(8)	-
10.0	-43.0372(2)	-43.0998(3)	-42.9157(5)	-	-
15.0	-43.0724(3)	-43.1036(3)	-42.927(1)	-	-

TABLE VI. Projected thermal energies obtained using our Monte Carlo method in the quantum Heisenberg limit for $L = 8$ at various values of β . The second column gives the ground-state energy obtained using $\mathbb{P}_{(1)}$. Because this subspace is free of sign problems, the single thermal energy $e_1(\beta)$ can be extracted accurately even at large β . The remaining four columns give the projected thermal energies obtained from \mathbb{P}_+ . Due to sign problems which sneak in from the larger projection subspace, we had to drop the projection state $|\psi_4\rangle$ at $\beta = 5$, and used only $|\psi_1\rangle$ and $|\psi_2\rangle$ at $\beta = 10, 15$. These results can be compared with the ground state energy of $-43.103168(256)$ in [40], the first excited state energy of $-42.90(4)$ and the second excited state energy of $-42.54(3)$ both obtained in [41].

lattices will give results similar to the $L = 4$ results. We have verified this at $L = 8$.

For $L = 8$, the ground state is the dimer state of Eq. (37), with energy $E_{\text{GS}} = -3JL^2/8$ which means $E_{\text{GS}} = -24$. We now examine whether we can compute the energy gap to the first excited state using the \mathbb{P}_- subspace, which now has $d_{\text{proj}} = 32$ as explained in Section VIB, should work well. Similar to the $L = 2$ and $L = 4$ cases, we again find empirically that $\langle \phi_a | e^{-\beta H} | \phi_c \rangle \propto \delta_{ac}$ to a good approximation in our Monte Carlo calculations, although now the sign problem manifests as large fluctuations even at $\beta = 1.0$. This indicates that the projected thermal energies obtained within this high-dimensional subspace are degenerate within Monte Carlo errors. We used a four-dimensional subspace within \mathbb{P}_- to compute this degenerate thermal energy levels, which should converge to the first excited-state energy in the limit of large β . We find it to be $-23.16(6)$ at $\beta = 0.75$. This results is also shown in Fig. 10. We see that $L = 4$ and $L = 8$ data are identical within errors as expected.

VII. CONCLUSIONS

In this work, we introduced a new Monte Carlo sampling approach for computing the projected low-energy spectrum of a general quantum Hamiltonian H . Our approach targets the subset of low-energy eigenstates $|\alpha\rangle$ of H that have nonzero overlap with a chosen d_{proj} -dimensional projection subspace \mathbb{P} , spanned by linearly independent states $|\psi_a\rangle$ ($a = 1, 2, \dots, d_{\text{proj}}$). As discussed in Section IV, this formulation enables the systematic identification of the projected low-energy eigenvalues \mathcal{E}_{α_a} directly from H and the chosen subspace. This provides a versatile numerical strategy that can be tailored to diverse quantum many-body systems.

Our Monte Carlo method enables the computation of the projected thermal energies $e_a(\beta)$, which smoothly approach the projected low-energy eigenvalues \mathcal{E}_{α_a} in the $\beta \rightarrow \infty$ limit. The method operates by evaluating two $d_{\text{proj}} \times d_{\text{proj}}$ matrices: the projected thermal density matrix Z and the corresponding projected thermal energy matrix E . All matrix elements are estimated through our Monte Carlo sampling procedure up to a common normalization factor, as is typical in such approaches. The projected thermal energies $e_a(\beta)$ are then obtained as the eigenvalues of the matrix product EZ^{-1} . We refer to this approach as the PDMS method.

Building on earlier concepts, our work establishes a systematic and broadly applicable framework that significantly extends previous Monte Carlo approaches. First, we sample the density matrix $e^{-\beta H}$ in continuous Euclidean time within the path-integral formulation, starting from a lattice quantum Hamiltonian in a finite Hilbert space. This eliminates Trotter errors and allows flexible exploration of different projection subspaces. Second, as demonstrated in this study, our method remains largely insensitive to sign problems at small values of β , enabling accurate evaluation of $e_a(\beta)$ even in highly frustrated regimes of the Shastry–Sutherland model (SSM). This robustness makes the technique suitable for a wide class of systems. Third, we show that with a judicious choice of projection subspaces, the projected thermal energies converge rapidly to the projected low-energy spectrum by providing reliable and accurate results even at small values of β .

As discussed in Section IV, both the precision and the rate of convergence of $e_a(\beta)$ toward the projected low-energy spectrum of H can be systematically improved, at fixed β , by carefully expanding the dimension d_{proj} of the projection subspace. We also introduced the concept of an ideal projection subspace for extracting a chosen set of d_{proj} projected low-energy levels. Such a subspace is

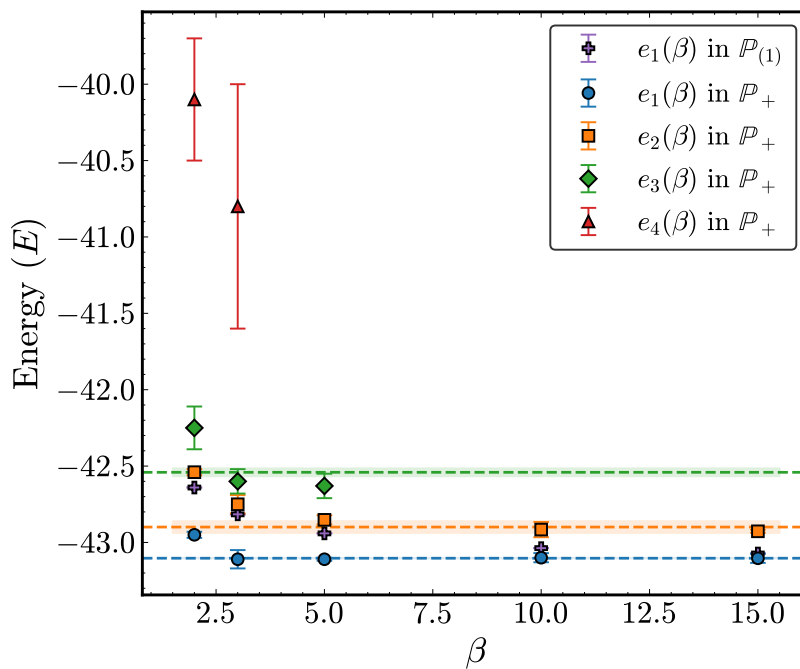


FIG. 9. Projected thermal energies for the 2D Heisenberg square lattice, at $L = 8$ as functions of inverse temperature β . The plus (purple) symbol shows the ground-state thermal energy $e_1(\beta)$ obtained within the single-state projection subspace $\mathbb{P}_{(1)}$, which is free of sign problems and thus yields accurate estimates even at large β . However, the results from this does not converge to the ground state (the lowest horizontal dashed line obtained in [40]). The other symbols display the projected thermal energies $e_i(\beta)$ ($i = 1, \dots, 4$) obtained from the full \mathbb{P}_+ . The circle symbol gives $e_1(\beta)$, which is already consistent with the ground state energy at $\beta = 3.0$. To avoid computational instabilities the projection state $|\psi_4\rangle$ was excluded from the analysis at $\beta = 5$, and only $|\psi_1\rangle$ and $|\psi_2\rangle$ were used at $\beta = 10, 15$. The higher two horizontal dashed lines are reference Monte Carlo results with their uncertainties (shaded bands) from the earlier study of Ref. [41]. These results demonstrate that (i) PDMS results converge to the ground state at very low β ; (ii) Comparing the blue circles with the purple plus markers, we learn that increasing the dimension of the projection subspace judiciously can considerably improve the rate of convergence.

characterized by the property that the corresponding projected eigenvectors of H form d_{proj} linearly independent vectors within the subspace, while all remaining projected eigenvectors have strictly higher energies. This idea provides a practical guideline for constructing efficient and well-targeted projection bases in future applications.

Using these analytic insights, we demonstrated in Sections V and VI that our method remains robust across a wide range of projection subspaces at high temperatures. In practice, we find that stable convergence close to the projected low-energy spectrum can often be achieved at moderate values of β , without encountering severe sign problems. At larger β or with significantly expanded projection subspaces, sign problems may reemerge, similar to the challenges faced when extracting higher-energy excitations in otherwise sign-problem-free systems [43]. These observations highlight the importance of carefully selecting projection subspaces that target the desired low-energy levels efficiently. We demonstrated this strategy successfully in our study of the transverse-field Ising model and $J = 0$ regime of the SSM, where well-chosen projection states enabled rapid and stable convergence.

A further strength of the PDMS framework is that the Monte Carlo sampling can, in principle, be formulated

in a variety of bases within the Hilbert space. In some cases, sign problems can be completely resolved through a careful choice of basis [39, 44], while in others they can be significantly mitigated [45]. It may also be possible to take guidance from analytic techniques such as perturbation theory when constructing the sampling basis. Furthermore, new ideas for addressing sign problems, such as meron clusters [24], fermion bags [46], exponential error reduction techniques using the multi-level blocking ideas [47–49], can all be naturally incorporated into our framework. These features showcase the broad adaptability of the method and its potential for integration with parallel advances in Monte Carlo methodology.

An interesting avenue for further development is the use of physically-motivated construction of projection states that are guided by the known quantum phases of the underlying Hamiltonian, as demonstrated in recent tensor-network studies [27]. For example, projection subspaces inspired by phase-specific wavefunctions, such as plaquette-valence-bond (PVB) type states in the Shastry–Sutherland model, may provide more efficient starting points for our PDMS method. Our preliminary results show that such physically motivated choices may considerably accelerate convergence and improve stability in

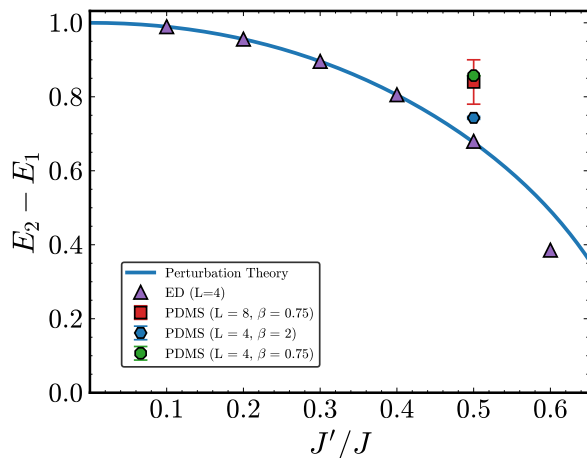


FIG. 10. The energy gap between the ground state (with energy E_1) and the first excited Triplet state (with energy E_2) plotted as a function of the coupling J'/J . The solid blue is obtained using perturbation theory up to $(J'/J)^{21}$ from Ref. [42]. The colored markers without errors are ED results from a 4×4 lattice. The agreement between ED and perturbative results confirms that non-perturbative effects remain small up to $J'/J \approx 0.5$. The data from our Monte Carlo method at $J'/J = 0.5$ for $L = 4$ (that also appear in Fig. 8) are shown to demonstrate the rate of convergence. We also show data from our Monte Carlo method at $J'/J = 0.5$, $L = 8$ and $\beta = 0.75$ and find that it agrees with the $L = 4$ data within errors.

challenging regimes. We plan to share these findings in a future work.

The PDMS framework naturally admits a physical interpretation in terms of an effective thermal system defined by the projected thermal density matrix. The corresponding effective energies $e_a(\beta)$ characterize this system at finite temperature, while their $\beta \rightarrow \infty$ limit yields the projected low-energy spectrum of H . Viewed in this way, our method provides a nonperturbative and efficient approach to exploring this effective thermal problem at high temperatures, where Monte Carlo simulations are most stable. Moreover, developing an analytic understanding of the β dependence of $e_a(\beta)$ may enable systematic extrapolations from high-temperature results to the low-temperature regime. This perspective is conceptually similar to finite-size scaling analyses, where controlled extrapolations from smaller systems can predict behavior in the thermodynamic limit. Establishing this connection more concretely presents a natural direction for future research.

Thus, by combining the aforementioned features and directions for further refinement, we believe that the PDMS method emerges as a powerful and versatile computational framework for determining the low-energy spectrum of generic quantum Hamiltonians. Its flexibility in defining projection subspaces, robustness against sign problems at low β , and compatibility with modern Monte Carlo and analytical techniques make it broadly relevant across diverse problems in quantum many-body physics. We

anticipate that the method will find applications not only in condensed-matter systems, such as frustrated magnets and quantum spin models demonstrated here, but also in lattice gauge theories formulated in the Hamiltonian framework. More broadly, we hope that this work will encourage the development of projection-based Monte Carlo strategies as a general paradigm for exploring complex quantum systems beyond the reach of traditional approaches.

ACKNOWLEDGMENTS

SC thanks Subhro Bhattacharjee, Souvik Kundu, and Indrajit Sau for collaboration on another project involving the PDMS method; discussions from that work have also influenced the progress reported here. SC is supported in part by the U.S. Department of Energy, Office of Science, Nuclear Physics program under Award No. DE-FG02-05ER41368. RKK and HSW were supported by the NSF under Award No. DMR-2312742. SC was also supported in part by the International Centre for Theoretical Sciences (ICTS) under its Associates Program, during which some of the ideas of the present work were developed. AK thanks Sara Haravifard and Lalit Yadav for introducing the exciting physics of the Shastry-Sutherland Model. AK is supported by funds from Duke University for this research.

Appendix A: Stochastic Series Expansion

While we chose to present our PDMS algorithm using a path integral formulation, it can equally well be formulated using the popular stochastic series expansion (SSE) [20]. The steps are self evident but are included here for completeness. To compute the Z matrix, we simply expand the exponential as usual in the SSE,

$$Z_{ac} = \langle \psi_a | e^{-\beta H} | \psi_c \rangle \quad (\text{A1})$$

$$= \sum_n \langle \psi_a | \frac{(-\beta H)^n}{n!} | \psi_c \rangle. \quad (\text{A2})$$

and insert complete sets of states between each H and then sample the various bond terms which H can be written as a sum of, Eq. 3. The updates are standard, there are both diagonal and off-diagonal updates, though now one has to allow for the possibility of the boundary states $|\psi_a\rangle$ and $|\psi_c\rangle$ to be updated, along the lines of what we have described in the path integral approach. The matrix E can also be constructed in this manner. Once both these matrices are constructed they can be analyzed exactly as described in our paper. Since the Monte Carlo sampling procedures are very similar, it is anticipated that the SSE formulation will not offer any significant advantages or disadvantages as compared to the path integral formulation we have formulated here,

r	$\langle\psi \alpha_0\rangle$	ψ -rep	$\langle\psi \alpha_1\rangle$	ψ -rep	$\langle\psi \alpha_2\rangle$	ψ -rep	$\langle\psi \alpha_3\rangle$	ψ -rep
1	0.6908	↑↑↑↑↑↑↑↑↑↑↑↑↑↑	0.3576	↑↑↑↑↑↑↑↑↑↑↑↑↑↑	0.3031	↓↓↓↓↓↓↓↓↓↓↓↓↓↓↓↑	0.4027	↓↓↓↓↓↓↓↓↓↓↓↓↓↓↓↓
2	0.5632	↓↑↑↑↑↑↑↑↑↑↑↑↑↑	0.3356	↓↓↓↑↑↑↑↑↑↑↑↑↑↑↑	0.2604	↑↑↑↑↑↑↑↑↑↑↑↑↑↑	0.3979	↓↓↓↓↓↓↓↓↓↓↓↓↓↓↓↑
3	0.2371	↓↓↑↑↑↑↑↑↑↑↑↑↑↑	0.3249	↓↓↓↓↑↑↑↑↑↑↑↑↑↑	0.2576	↓↓↓↓↓↓↓↓↓↓↓↓↓↓↓↓	0.3004	↓↓↓↓↓↑↑↑↑↑↑↑↑↑↑
4	0.1363	↓↑↓↑↑↑↑↑↑↑↑↑↑↑↑	0.2701	↓↓↓↓↓↑↑↑↑↑↑↑↑↑↑	0.2539	↓↓↑↑↑↑↑↑↑↑↑↑↑↑	0.2884	↓↓↓↓↓↓↓↓↓↑↑↑↑↑↑↑

TABLE VII. The zero-momentum Z -basis states $|\psi\rangle$ with the largest overlap with the energy eigenstates $|\alpha\rangle$. A representative for the $k = 0$ state $|\psi\rangle$ is given, from which the full state is constructed via symmetrization. Only the $r = 4$ state for $|\alpha_0\rangle$ lies outside the 0 and 2 domain wall sector.

indeed apart from some book-keeping, both methods are quite similar.

Appendix B: Details: Transverse Field Ising Model

In this appendix, we provide further details of our calculations related to the application of the PDMS to the TFIM.

1. Projection subspace

Our choice of the projection subspace, \mathbb{P} , was made using data from exact diagonalization results on small lattices. We explored which Z -basis states have the highest overlap with the lowest energy eigenstates of H . In Table VII we show the four largest overlaps between zero-momentum Z -basis states and the exact energy eigenstates for $L = 12$ and $h = 0.2$. We see that all but one state ($r = 4$ for $|\alpha_0\rangle$) falls within the zero or two domain wall sectors. This motivated us to focus on states of the form $|\psi_{\ell+2}\rangle$ defined in Eq. (29). While there are clearly large overlaps with these states for $L/2 < \ell < L$, we only focused on the states where $1 < \ell \leq L/2$ in order to reduce the dimension of \mathbb{P} . This restricted space continues to be a good choice. Motivated by the largest overlap seen for the fourth excited state we added the state Eq. (28) where all the spins were flipped. On large lattices this state is clearly not necessary.

2. Zero modes of Z

The extraction of the projected thermal energies $e_a(\beta)$ relies on inverting the matrix \hat{Z} . While the exact eigenvalues of \hat{Z} are guaranteed to be positive, this is not true in the presence of Monte Carlo error. Since the eigenvalue ratios are expected to be of the form $e^{-\beta(\mathcal{E}_a - \mathcal{E}_0)}$, for higher energy modes at low temperatures, eigenvalues of \hat{Z} can become indistinguishable from zero (within errors). In this case we encounter a “zero mode”, obstructing the extraction of *any* projected energies.

One naïve strategy is to take a smaller projection subspace with dimension approximately equal to the number of low energy modes we are targeting. However, we find that taking a small projection subspace drastically slows

the convergence to the $\beta \rightarrow \infty$ energies, making this strategy unfeasible for extracting the projected low energy spectrum. Moreover, this does not necessarily mitigate the zero mode issue.

We have discovered that a better approach is to keep a large projection subspace, but then *further project* into the subspace of \hat{Z} that is zero-mode free as we explained in Section IV. In this approach we diagonalize Z/Z^b and then project both Z/Z^b and \hat{E}/Z^b to a lower dimensional subspace of dimension $d_{\text{proj}}^{\text{res}}$, such that Z/Z^b is strictly positive in this lower dimensional subspace. The projected thermal energies $e_a(\beta)$ are then well defined.

A natural question to ask is how the projection from the original d_{proj} dimensional subspace to the smaller $d_{\text{proj}}^{\text{res}}$ subspace affects the projected thermal energies. We have explored this question by comparing exact diagonalization results with results obtained from Monte Carlo at $L = 12$ and with a $d_{\text{proj}} = 8$. In the left panel of Fig. 11, we show the exact diagonalization results for the effect of lowering $d_{\text{proj}}^{\text{res}}$. We find that the effect is relatively mild with the projected energies staying close to the zero temperature results (dashed lines). In the right panel of Fig. 11 we plot the results for the projected thermal energies as a function of β obtained using the Monte Carlo method, and focus on $d_{\text{proj}}^{\text{res}} = 6$. We observe that the Monte Carlo errors increase with β for the highest two energies and this makes it difficult to extract reliable results at $\beta = 1.4$. If pushed to higher β , the Z/Z^b will encounter a zero mode, obstructing energy extraction. In contrast we can even reach $\beta = 1.8$ if we use $d_{\text{proj}}^{\text{res}} = 4$. This shows that if $d_{\text{proj}}^{\text{res}}$ is too high, small eigenvalues arising from higher energy states can substantially contribute to the errors in the lower energy levels.

Appendix C: Details: Shastry Sutherland Model

In this appendix, we provide details related to Section V to help a reader follow the discussion.

1. Lattice Details

We first define the $\langle ij \rangle$ and $\langle\langle ij \rangle\rangle$ bonds that appear in the Hamiltonian more carefully. This helps us set up the notation that we use when to define the projection subspaces. We label each lattice site by its coordinates

index (a)	$E_a(s)(g)$			
	$(J = 0, J' = 1)$	$(J = 1, J' = 0.5)$	$(J = 1, J' = 0.66)$	$(J = 1, J' = 0.75)$
1	-4.00(0)(1)	-1.50(0)(2)	-2.14(0)(1)	-2.50(0)(1)
2	-2.00(1)(1)	-0.50(1)(3)	-1.50(0)(1)	-1.50(0)(1)
3	0.00(0)(1)	1.50(2)(1)	-0.82(1)(1)	-1.00(1)(1)
4	0.00(1)(2)		-0.50(1)(2)	-0.50(1)(2)
5	2.00(2)(1)		1.82(2)(1)	2.00(2)(1)

TABLE VIII. Distinct energy levels of H for $L = 2$, listed in ascending order at four different coupling values. The leftmost column gives the index a for each distinct energy level E_a . The remaining four columns show $E_a(s)(g)$ at the corresponding couplings (J, J') . Here s denotes the spin representation and g is the degeneracy associated with that representation. The total degeneracy of level E_a is therefore $g(2s + 1)$.

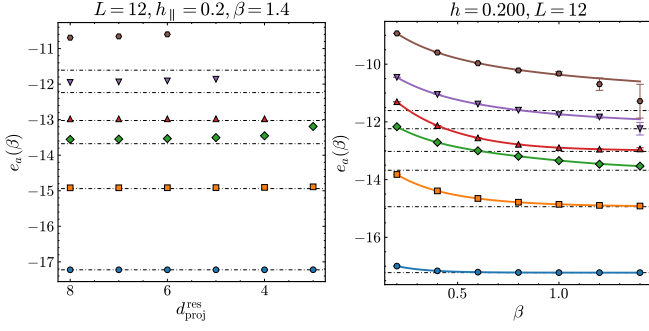


FIG. 11. (a) Exact diagonalization study of projected energies as a function of $d_{\text{proj}}^{\text{res}}$ for a fixed projected subspace of dimension $d_{\text{proj}} = 8$ (b) PDMS energies as a function of β with $d_{\text{proj}}^{\text{res}} = 6$ and $d_{\text{proj}} = 8$.

(x_i, y_i) , where $x_i, y_i = 0, 1, \dots, L - 1$. Sites for which $x_i + y_i$ is even (odd) are referred to as even (odd) sites. The $\langle ij \rangle$ bonds denote nearest-neighbor pairs, where we always choose i to be an even site and j to be the corresponding odd neighbor. The $\langle\langle ij \rangle\rangle$ bonds form a specific set of diagonal pairs, where both i and j are either even sites ($\langle\langle ij \rangle\rangle_A$ bonds) or odd sites ($\langle\langle ij \rangle\rangle_B$ bonds). In the $\langle\langle ij \rangle\rangle_A$ case, i has even x_i , and j is chosen with coordinates $x_j = x_i + 1$ and $y_j = y_i + 1$. In the $\langle\langle ij \rangle\rangle_B$ case, i again has even x_i , while j has $x_j = x_i - 1$ and $y_j = y_i + 1$. Periodic boundary conditions are imposed when coordinates cross the lattice boundaries. These definitions ensure that the $\langle\langle ij \rangle\rangle$ bonds partition the L^2 sites uniquely into two sets of $L^2/2$ bonds. All these features are illustrated on an $L = 4$ lattice in Fig. 6.

2. Definitions of local states

We construct our projection subspaces using unnormalized singlet and triplet dimer states on the $\langle ij \rangle$ and $\langle\langle ij \rangle\rangle$ bonds. The singlet dimers are defined as

$$|\psi_s\rangle = (-1)^{x_i + y_i} (|\uparrow\rangle_i \otimes |\downarrow\rangle_j - |\downarrow\rangle_i \otimes |\uparrow\rangle_j), \quad (\text{C1})$$

and the triplet dimers are defined as

$$|\psi_t\rangle = (|\uparrow\rangle_i \otimes |\downarrow\rangle_j + |\downarrow\rangle_i \otimes |\uparrow\rangle_j), \quad (\text{C2})$$

where we assume $|\uparrow\rangle_i$ and $|\downarrow\rangle_i$ to be eigenstates of the s_i^z with eigenvalues $+1/2$ and $-1/2$. In the singlet definition, the phase factor $(-1)^{x_i + y_i}$ depends on site i , which was defined uniquely above when specifying the $\langle ij \rangle$ and $\langle\langle ij \rangle\rangle$ bonds.

3. Exact results for $L = 2$

For $L = 2$ we can use the dimer basis introduced in Section VI to construct the states. This dimer basis consists of a triplet state $|m\rangle$ ($m = \pm 1, 0$) or a singlet state $|s\rangle$ on each of the two diagonal bonds of the lattice. The first bond connects the sites with coordinates $(x, y) = (0, 0)$ and $(1, 1)$, while the second connects $(0, 1)$ and $(1, 0)$. Thus, the full 16-dimensional Hilbert space in this basis consists of 9 states labeled $|m; m'\rangle$, 3 states labeled $|m; s\rangle$, 3 labeled $|s; m\rangle$, and a single state $|s; s\rangle$.

In this dimer basis, the five $s = 2$ eigenstates of the SSM are

$$|\chi_1\rangle = | + 1; + 1 \rangle, \quad (\text{C3})$$

$$|\chi_2\rangle = \frac{1}{\sqrt{2}} (| + 1; 0 \rangle + | 0; + 1 \rangle), \quad (\text{C4})$$

$$|\chi_3\rangle = \frac{1}{\sqrt{6}} (| + 1; - 1 \rangle + | - 1; + 1 \rangle + 2| 0; 0 \rangle), \quad (\text{C5})$$

$$|\chi_4\rangle = \frac{1}{\sqrt{2}} (| - 1; 0 \rangle + | 0; - 1 \rangle), \quad (\text{C6})$$

$$|\chi_5\rangle = | - 1; - 1 \rangle, \quad (\text{C7})$$

and have energy $2J' + J/2$.

In addition, there are three $s = 1$ (triplet) eigenstates formed with triplets on both diagonal bonds:

$$|\chi_6\rangle = \frac{1}{\sqrt{2}} (| 0; + 1 \rangle - | + 1; 0 \rangle), \quad (\text{C8})$$

$$|\chi_7\rangle = \frac{1}{\sqrt{2}} (| + 1; - 1 \rangle - | - 1; + 1 \rangle), \quad (\text{C9})$$

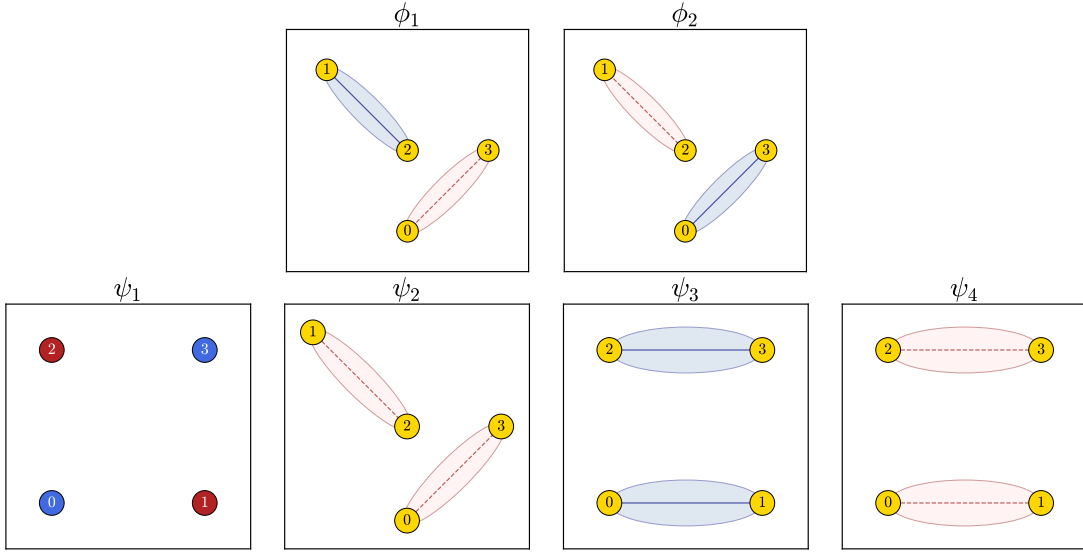


FIG. 12. The top two panels show the two projection states in the \mathbb{P}_- subspace on a $L = 2$ lattice. The bottom four panels show the four projection states in the \mathbb{P}_+ subspace on a $L = 2$ lattice. The blue circle denote the state $(|\uparrow\rangle + |\downarrow\rangle)$, the red circle denotes the state $(|\downarrow\rangle - |\uparrow\rangle)$, the dashed dimers represent $|\psi_t\rangle$, and the solid dimers represent $|\psi_s\rangle$ as defined in Eqs. (C1) and (C2).

$$|\chi_8\rangle = \frac{1}{\sqrt{2}}(|0; -1\rangle - |-1; 0\rangle), \quad (\text{C10})$$

with energy $-2J' + J/2$.

The next two triplets are formed using one diagonal triplet and one diagonal singlet:

$$|\chi_{10}\rangle = |+1; s\rangle, \quad |\chi_{11}\rangle = |0; s\rangle, \quad |\chi_{12}\rangle = |-1; s\rangle, \quad (\text{C11})$$

$$|\chi_{13}\rangle = |s; +1\rangle, \quad |\chi_{14}\rangle = |s; 0\rangle, \quad |\chi_{15}\rangle = |s; -1\rangle, \quad (\text{C12})$$

and both sets are degenerate with energy $-J/2$.

Finally, there are two singlets. The first is formed from two diagonal triplets:

$$|\chi_9\rangle = \frac{1}{\sqrt{3}}(|0; 0\rangle - |+1; -1\rangle - |-1; +1\rangle), \quad (\text{C13})$$

with energy $-4J' + J/2$, while the second is formed from two diagonal singlets:

$$|\chi_{16}\rangle = |s; s\rangle, \quad (\text{C14})$$

with energy $-3J/2$. These energies at the four couplings we study in this work are given in Table VIII.

We can now compute the overlap of these energy eigenstates with the projection states spanning the $Q = +1$ and $Q = -1$ projection subspaces. The basis state $|\psi_1\rangle$ in the $Q = +1$ subspace is

$$|\psi_1\rangle = |+1; +1\rangle + |-1; -1\rangle - 2|0; 0\rangle + |-1; +1\rangle + \sqrt{2}(|0; +1\rangle - |+1; 0\rangle + |0; -1\rangle - |-1; 0\rangle), \quad (\text{C15})$$

which, when expressed in terms of the eigenstates of H , becomes

$$|\psi_1\rangle = |\chi_1\rangle + |\chi_5\rangle + 2(|\chi_6\rangle + |\chi_8\rangle) - \sqrt{\frac{2}{3}}|\chi_3\rangle - \frac{4}{\sqrt{3}}|\chi_9\rangle. \quad (\text{C16})$$

The other three states in the same subspace are

$$|\psi_2\rangle = 2|0; 0\rangle = \sqrt{\frac{8}{3}}|\chi_3\rangle + \frac{2}{\sqrt{3}}|\chi_9\rangle, \quad (\text{C17})$$

$$|\psi_3\rangle = |+1; -1\rangle + |-1; +1\rangle - |0; 0\rangle + |s; s\rangle = -\sqrt{3}|\chi_9\rangle + |\chi_{16}\rangle, \quad (\text{C18})$$

$$|\psi_4\rangle = |+1; -1\rangle + |-1; +1\rangle + |0; 0\rangle - |s; s\rangle = \frac{4}{\sqrt{6}}|\chi_3\rangle - \frac{1}{\sqrt{3}}|\chi_9\rangle - |\chi_{16}\rangle. \quad (\text{C19})$$

The two states in the $Q = -1$ projection subspace are

$$|\phi_1\rangle = |\psi_5\rangle = 2|0; s\rangle = 2|\chi_{11}\rangle, \quad (\text{C20})$$

$$|\phi_2\rangle = 2|s; 0\rangle = 2|\chi_{14}\rangle. \quad (\text{C21})$$

Note that these are already exact eigenstates of H . We can use the above information to obtain the information given in Tables III and VIII. Fig. 12 gives a pictorial illustration of \mathbb{P}_+ and \mathbb{P}_- subspaces for $L = 2$.

4. Exact Results for $L = 4$

Here we list the exact energies obtained using exact diagonalization and provide information about the overlap of the projection states $|\psi_1\rangle$, $|\psi_2\rangle$, $|\psi_3\rangle$ and $|\psi_4\rangle$, in the \mathbb{P}_+ subspace and $|\phi_1\rangle$ in the \mathbb{P}_- subspace with the

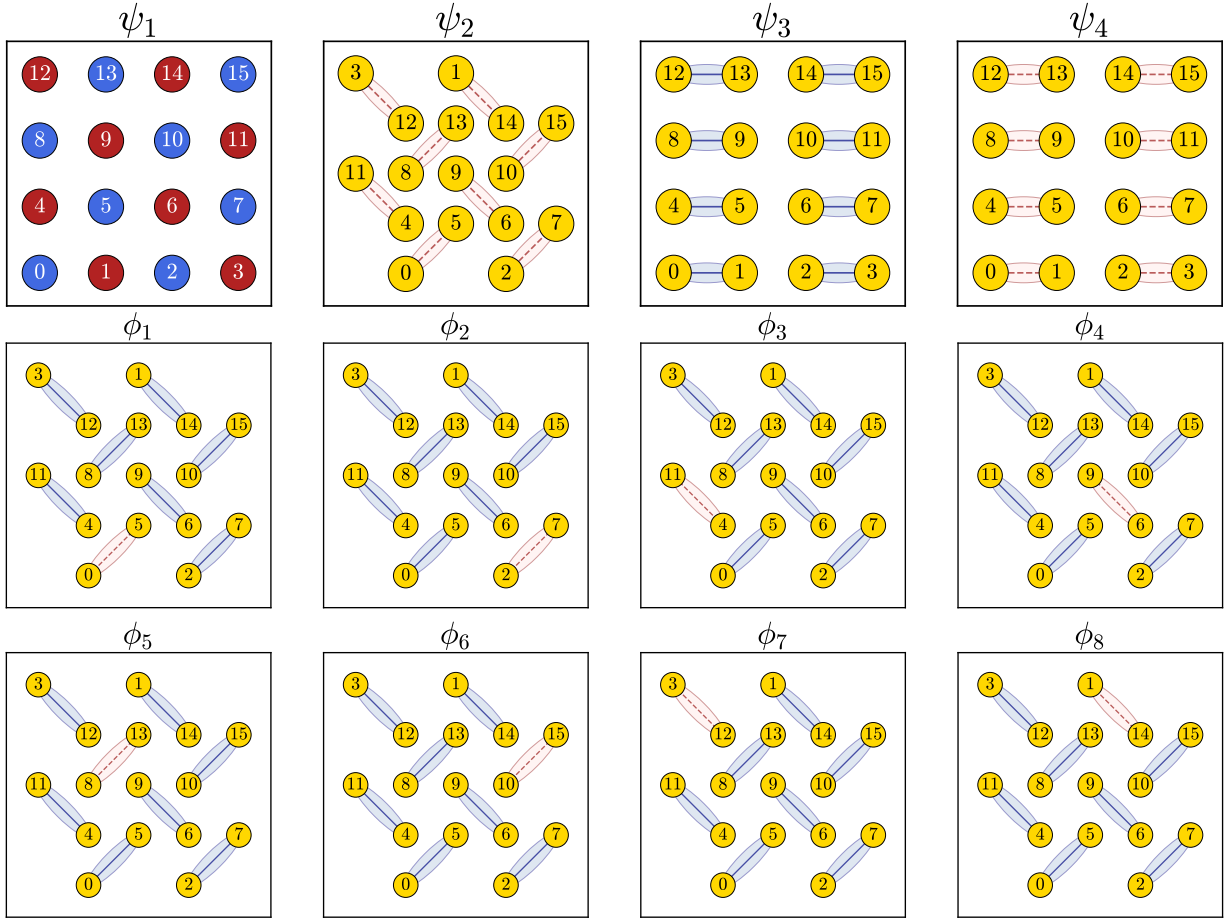


FIG. 13. The top row shows the four projection states in the \mathbb{P}_+ subspace on a $L = 4$ lattice. The bottom two rows show the eight projection states in the \mathbb{P}_- subspace on a $L = 4$ lattice. The definitions of the bonds are the same as in Fig. 12.

energy eigenstates of H . The remaining seven projection states in the \mathbb{P}_- subspace have very similar projections as $|\phi_1\rangle$.

Focusing first on the distinct energy levels of H , we use exact diagonalization to find them all. Although the total Hilbert space is considerably larger than the $L = 2$ case, with dimension $2^{16} = 65,536$, we can restrict our calculation to the subspace of eigenstates of H with total $s^z = 0$, which contains only 12,870 states. This reduced Hamiltonian matrix can be diagonalized easily. Likewise, we can analyze each $s^z \neq 0$ sector separately, obtaining smaller matrices that can also be diagonalized, thereby yielding all eigenvalues and eigenvectors of H . We can compute s by diagonalizing the S^2 operator in each degenerate subspace, since $[S^2, H] = 0$. The first 45 distinct levels that we find are listed in Table IX. Fig. 13 gives a pictorial illustration of \mathbb{P}_+ and \mathbb{P}_- subspaces for $L = 4$.

In order to find the projected low energy spectrum in the two subspaces, we next compute the overlap of the projection states with various energy eigenstates. In Table X we give the overlap of $|\phi_1\rangle$ and in Table XI we give the overlap with $|\psi_1\rangle$, $|\psi_2\rangle$, $|\psi_3\rangle$ and $|\psi_4\rangle$.

index (a)	$E_a(s)(g)$			
	$(J = 0, J' = 1)$	$(J = 1, J' = 0.5)$	$(J = 1, J' = 0.66)$	$(J = 1, J' = 0.75)$
1	-11.228483(0)(1)	-6.000000(0)(1)	-6.000000(0)(1)	-6.884403(0)(1)
2	-10.649885(1)(1)	-5.320287(1)(4)	-5.933096(0)(1)	-6.443055(0)(2)
3	-9.517688(2)(1)	-5.320042(1)(4)	-5.916800(0)(2)	-6.370229(1)(1)
4	-8.886442(1)(4)	-5.182600(0)(2)	-5.782810(0)(4)	-6.252202(0)(4)
5	-8.794379(1)(4)	-5.117269(0)(4)	-5.645621(1)(4)	-6.152386(1)(4)
6	-8.518284(1)(6)	-5.029625(0)(1)	-5.642281(0)(1)	-6.056300(1)(4)
7	-8.252827(0)(3)	-5.027025(0)(1)	-5.639354(1)(4)	-6.043823(0)(1)
8	-7.877905(0)(8)	-5.026103(0)(2)	-5.632751(0)(2)	-6.031847(0)(1)
9	-7.836538(3)(1)	-5.019828(0)(2)	-5.628946(0)(1)	-6.022370(1)(4)
10	-7.812148(0)(6)	-4.812839(0)(1)	-5.587025(0)(2)	-6.000000(0)(1)
11	-7.765674(2)(4)	-4.804425(1)(4)	-5.506831(1)(4)	-5.999654(0)(2)
12	-7.687234(0)(1)	-4.802876(1)(4)	-5.487639(1)(2)	-5.968997(0)(4)
13	-7.630213(2)(4)	-4.793562(1)(2)	-5.439011(0)(1)	-5.964137(1)(2)
14	-7.477053(2)(6)	-4.778225(1)(2)	-5.438800(1)(1)	-5.953098(0)(2)
15	-7.432605(1)(6)	-4.769293(0)(4)	-5.422847(1)(4)	-5.895058(1)(4)
16	-7.389958(1)(8)	-4.769273(0)(4)	-5.394965(1)(4)	-5.892307(0)(4)
17	-7.374398(1)(3)	-4.650356(1)(2)	-5.367820(0)(4)	-5.891210(0)(4)
18	-7.128523(0)(6)	-4.632985(1)(4)	-5.341862(0)(4)	-5.857640(0)(2)
19	-6.974804(0)(4)	-4.631229(0)(1)	-5.339562(0)(4)	-5.826138(0)(1)
20	-6.910831(0)(4)	-4.627777(2)(2)	-5.338550(0)(2)	-5.819339(1)(4)
21	-6.776769(2)(3)	-4.613176(1)(4)	-5.306673(1)(2)	-5.801340(0)(1)
22	-6.759607(0)(3)	-4.606503(0)(4)	-5.301164(1)(4)	-5.783725(1)(4)
23	-6.735370(1)(6)	-4.602550(2)(1)	-5.220173(1)(4)	-5.760944(1)(4)
24	-6.671460(1)(6)	-4.594634(2)(4)	-5.219546(1)(4)	-5.674710(1)(2)
25	-6.659101(1)(4)	-4.567206(1)(4)	-5.173984(1)(2)	-5.638308(0)(2)
26	-6.632900(1)(1)	-4.504516(0)(2)	-5.168376(0)(1)	-5.617886(1)(2)
27	-6.587695(1)(4)	-4.485153(1)(2)	-5.165203(1)(4)	-5.610840(0)(1)
28	-6.584650(0)(8)	-4.466332(2)(1)	-5.109319(0)(1)	-5.607030(1)(4)
29	-6.515256(0)(6)	-4.462375(1)(4)	-5.108918(0)(4)	-5.589100(1)(4)
30	-6.495976(2)(6)	-4.454945(1)(4)	-5.106297(2)(1)	-5.523017(1)(4)
31	-6.452904(2)(3)	-4.421657(1)(4)	-5.099047(2)(2)	-5.510477(0)(4)
32	-6.447382(0)(4)	-4.373617(0)(1)	-5.078950(1)(4)	-5.499922(2)(1)
33	-6.386656(1)(8)	-4.328330(1)(4)	-5.073168(0)(4)	-5.480655(0)(4)
34	-6.371225(2)(6)	-4.307419(2)(4)	-5.065864(2)(4)	-5.473585(1)(1)
35	-6.290827(1)(4)	-4.303792(0)(2)	-5.063913(1)(4)	-5.455337(2)(1)
36	-6.271618(1)(2)	-4.301528(2)(4)	-5.058290(1)(4)	-5.446136(1)(4)
37	-6.269614(1)(8)	-4.293005(1)(1)	-5.016248(0)(1)	-5.436872(0)(1)
38	-6.263645(2)(8)	-4.286496(0)(4)	-5.001478(0)(4)	-5.436555(2)(2)
39	-6.231479(2)(1)	-4.280238(0)(4)	-4.995843(0)(2)	-5.425527(1)(1)
40	-6.229928(1)(8)	-4.273400(1)(1)	-4.994059(1)(1)	-5.405521(1)(4)
41	-6.195617(2)(8)	-4.254363(2)(2)	-4.990596(1)(1)	-5.400260(1)(4)
42	-6.176941(2)(8)	-4.252526(0)(4)	-4.981097(1)(2)	-5.394346(2)(4)
43	-6.173178(1)(6)	-4.245270(2)(1)	-4.940270(0)(4)	-5.388913(1)(2)
44	-6.148869(3)(4)	-4.244846(2)(1)	-4.930326(1)(4)	-5.352229(0)(2)
45	-6.110109(1)(3)	-4.244222(2)(2)	-4.917262(1)(4)	-5.324424(0)(4)

TABLE IX. Distinct energy levels of H for $L = 4$, listed in ascending order at four different coupling values. The notation follows that of Table VIII.

Projection State	(J=0, J'=1)		(J=1, J'=0.5)		(J=1, J'=0.66)		(J=1, J'=0.75)	
	(a)	$\langle \chi_a \phi_1 \rangle$	(a)	$\langle \chi_a \phi_1 \rangle$	(a)	$\langle \chi_a \phi_1 \rangle$	(a)	$\langle \chi_a \phi_1 \rangle$
$ \psi_5\rangle$	4	-0.000523	2	-2.103814	5	-5.206269	5	-0.674330
	4	-0.000417	2	+3.151237	5	-3.555676	5	+0.113756
	4	+0.000049	2	+8.303796	5	-0.898546	5	+0.382555
	4	-0.000396	2	+1.254938	5	+0.179952	5	-0.342496
	5	+0.000208	3	-1.583050	7	-6.407277	6	-0.281432
	5	-0.000080	3	+6.913795	7	+0.422894	6	-1.030326
	5	-0.000112	3	-2.804170	7	+0.680648	6	+1.642171
	5	-0.000163	3	+5.180237	7	+0.830089	6	+0.604951
	6	+0.000176	11	+0.030649	15	+1.920424	15	-3.035473
	6	-0.000298	11	+0.084143	15	+2.589075	15	-1.346833
	6	+0.000825	11	+0.028422	15	-1.037317	15	+2.433828
	6	+0.000158	11	-0.009558	15	-0.542344	15	+0.066491
	6	+0.000392	18	+1.201394	16	-0.680921	20	-0.224009
	6	+0.000159	18	+1.229969	16	-3.302649	20	+2.456945
	15	-0.001336	18	-3.925980	16	+1.427879	20	+1.640985
	15	-0.002694	18	-2.040563	16	+1.654346	20	+1.696154
	15	-0.001904	21	+3.598485	22	-0.012883	22	+0.110409
	15	-0.001241	21	+1.199243	22	-0.748783	22	+2.470518
	15	+0.000172	21	-2.574054	22	-0.412948	22	-1.564518
	15	-0.001100	21	+1.990788	22	+0.876721	22	+2.555769
	16	+0.001002	29	-1.803682	23	+0.035347	23	+1.701200
	16	-0.001189	29	-0.794814	23	-0.180211	23	+2.251446
	16	+0.000731	29	-0.045448	23	+2.228450	23	-0.354720
	16	+0.000611	29	-0.553695	23	+0.831433	23	-2.055897
	16	-0.001217	31	-0.083550	24	+0.232138	28	-0.487518
	16	-0.001145	31	+1.434149	24	-0.385640	28	-0.109098
	16	+0.000989	31	+0.537135	24	-0.088382	28	+0.421335
	16	+0.000466	31	-1.359334	24	-0.515504	28	+0.208351
	23	-0.001943	33	+0.952714	32	-1.168784	30	-0.371020
	23	+0.000012	33	-0.973504	32	+3.279464	30	-1.407949
	23	+0.002799	33	+0.208153	32	+0.171437	30	-1.945576
	23	-0.000229	33	+0.721085	32	-0.066812	30	-0.642030

TABLE X. Overlap of the projection state $|\phi_1\rangle$ in the $Q = -1$ projection subspace with the lowest distinct energy eigenstates $|\chi_a\rangle$ (up to some high energy cutoff) at the different couplings.

Reference State	(J=0, J'=1)		(J=1, J'=0.5)		(J=1, J'=0.66)		(J=1, J'=0.75)	
	(a)	$\langle \chi_a \psi_i \rangle$	(a)	$\langle \chi_a \psi_i \rangle$	(a)	$\langle \chi_a \psi_i \rangle$	(a)	$\langle \chi_a \psi_i \rangle$
$ \psi_1\rangle$	1	-73.572245	6	+1.029357	2	+51.797366	1	-58.563070
	2	-81.545673	32	+28.703482	9	+17.469325	3	-70.038105
	2	-81.545673	44	-0.270035	14	-67.036584	3	+70.038105
	3	+60.170614	44	-0.270035	14	+67.036584	8	+17.009229
	3	-73.693652	44	+0.220483	37	-38.647933	27	+35.546385
	3	-73.693652					32	-62.463940
	9	-57.258901					32	+51.001593
	9	-57.258901					32	+62.463940
	9	-44.352554						
	9	+44.352554						
	12	+32.818994						
	26	-40.137590						
	26	+40.137590						
	39	+11.323668						
	39	+11.323668						
	39	+9.245737						
$ \psi_2\rangle$	1	-0.887215	6	+0.007772	2	+0.558333	1	-0.647766
	3	+1.062861	32	+0.277715	9	+0.205151	8	+0.232299
	12	+0.831569	44	+0.004085	37	-0.533194	27	+0.533529
	31	-0.029389					32	+0.848457
	31	+1.575769						
	31	-1.290705						
	39	+0.771978						
$ \psi_3\rangle$	1	-4.771500	1	-0.250000	1	-0.250000	1	-6.014836
	7	-6.843183	4	+0.000515	2	+6.113502	2	+0.776693
	7	-3.955590	4	+0.173052	3	+0.113003	2	-4.397768
	7	-2.793187	6	-0.681085	3	-2.694568	7	+0.092138
	12	-4.663593	7	+1.146214	6	-0.995001	8	+0.289489
	22	-2.263543	26	+4.154496	9	+2.016729	10	+0.250000
	22	-2.751587	26	-0.661060	20	-6.759096	18	+2.428977
	22	-0.465120	32	+7.003587	20	+0.652893	18	-5.466307
			35	-1.599671	26	-3.417394	21	-3.906933
			35	-3.784518	37	+3.184226	27	-3.945731
							44	-0.909664
						44	-0.085537	
$ \psi_4\rangle$	1	-0.253664	1	-0.250000	1	-0.250000	1	-0.381669
	3	-0.448050	4	+0.000920	2	+0.404230	2	-0.015514
	7	+0.574956	4	+0.309110	3	+0.003757	2	+0.087845
	7	+0.332344	6	-0.332405	3	-0.089582	7	-0.224484
	7	+0.234680	7	+0.003566	6	-0.085798	8	+0.095751
	12	-0.411226	20	-0.011440	9	+0.320786	10	+0.250000
	21	+0.426513	20	+0.241323	20	+0.660340	18	-0.283768
	21	+0.046423	26	-0.453246	20	-0.063785	18	+0.638608
	21	+0.970522	26	+0.072120	26	+0.438696	21	+0.386064
	22	-0.206410	32	+0.788283	31	+0.081155	27	-0.739562
	22	-0.250914	35	+0.086646	31	-0.276906	32	-0.337693
	22	-0.042414	35	+0.204989	37	+0.702255	38	+0.008725
	39	+0.052647	43	+0.186901			38	-0.461112
			44	-0.343425			44	-0.418365
							44	-0.039339

TABLE XI. Overlaps of the four projection states that span the $Q = +1$ projection subspace with the lowest distinct eigenstates $|\chi_a\rangle$ (up to some high energy cutoff) at the different couplings.

- [1] M. C. Bañuls, Tensor network algorithms: A route map, *Annual Review of Condensed Matter Physics* **14**, 173 (2023).
- [2] M. Troyer and U.-J. Wiese, Computational complexity and fundamental limitations to fermionic quantum monte carlo simulations, *Physical Review Letters* **94**, 170201 (2005).
- [3] V. I. Iglovikov, E. Khatami, and R. T. Scalettar, Geometry dependence of the sign problem in quantum monte carlo simulations, *Physical Review B* **92**, 045110 (2015).
- [4] D. Hangleiter, I. Roth, D. Nagaj, and J. Eisert, Easing the monte carlo sign problem, *Science Advances* **5**, eaay7994 (2019).
- [5] G. Pan and Z. Y. Meng, The sign problem in quantum monte carlo simulations, in *Encyclopedia of Condensed Matter Physics*, edited by T. Chakraborty (Academic Press, Oxford, 2024) second edition ed., pp. 879–893.
- [6] B. Blossier, M. Della Morte, G. von Hippel, T. Mendes, and R. Sommer, On the generalized eigenvalue method for energies and matrix elements in lattice field theory, *JHEP* **04**, 094.
- [7] M. Luscher and U. Wolff, How to Calculate the Elastic Scattering Matrix in Two-dimensional Quantum Field Theories by Numerical Simulation, *Nucl. Phys. B* **339**, 222 (1990).
- [8] T. DeGrand and C. DeTar, *Lattice Methods for Quantum Chromodynamics* (WORLD SCIENTIFIC, 2006) <https://www.worldscientific.com/doi/pdf/10.1142/6065>.
- [9] A. Esposito, A. Pilloni, and A. D. Polosa, Multiquark Resonances, *Phys. Rept.* **668**, 1 (2017), [arXiv:1611.07920 \[hep-ph\]](https://arxiv.org/abs/1611.07920).
- [10] Y.-R. Liu, H.-X. Chen, W. Chen, X. Liu, and S.-L. Zhu, Pentaquark and Tetraquark states, *Prog. Part. Nucl. Phys.* **107**, 237 (2019), [arXiv:1903.11976 \[hep-ph\]](https://arxiv.org/abs/1903.11976).
- [11] R. G. Melko, A. B. Kallin, and M. B. Hastings, Finite-size scaling of mutual information in monte carlo simulations: Application to the spin-1/2 xxz model, *Phys. Rev. B* **82**, 100409 (2010).
- [12] C.-M. Chung, L. Bonnes, P. Chen, and A. M. Läuchli, Entanglement spectroscopy using quantum monte carlo, *Phys. Rev. B* **89**, 195147 (2014).
- [13] B.-B. Mao, Y.-M. Ding, Z. Wang, S. Hu, and Z. Yan, Sampling reduced density matrix to extract fine levels of entanglement spectrum and restore entanglement hamiltonian, *Nature Communications* **16**, 2880 (2025).
- [14] S. Chandrasekharan, S. T. Nguyen, and T. R. Richardson, Worldline Monte Carlo method for few-body nuclear physics, *Phys. Rev. C* **110**, 024002 (2024), [arXiv:2402.15377 \[nucl-th\]](https://arxiv.org/abs/2402.15377).
- [15] S. Chandrasekharan, Qubit Regularization of Quantum Field Theories, *PoS LATTICE2024*, 001 (2025).
- [16] B. B. Beard and U. J. Wiese, Simulations of discrete quantum systems in continuous Euclidean time, *Phys. Rev. Lett.* **77**, 5130 (1996), [arXiv:cond-mat/9602164](https://arxiv.org/abs/cond-mat/9602164).
- [17] E. Gull, A. J. Millis, A. I. Lichtenstein, A. N. Rubtsov, M. Troyer, and P. Werner, Continuous-time monte carlo methods for quantum impurity models, *Rev. Mod. Phys.* **83**, 349 (2011).
- [18] C.-J. Huang, L. Liu, Y. Jiang, and Y. Deng, Worm-algorithm-type simulation of the quantum transverse-field ising model, *Phys. Rev. B* **102**, 094101 (2020).
- [19] A. W. Sandvik, Stochastic series expansion method with operator-loop update, *Physical Review B* **59**, R14157 (1999).
- [20] A. W. Sandvik, Computational studies of quantum spin systems, in *AIP Conference Proceedings*, Vol. 1297 (AIP, 2010) pp. 135–338.
- [21] A. W. Sandvik, *Stochastic series expansion methods* (2019).
- [22] N. Prokof'ev and B. Svistunov, Worm algorithms for classical statistical models, *Phys. Rev. Lett.* **87**, 160601 (2001).
- [23] H. G. Evertz, The Loop algorithm, *Adv. Phys.* **52**, 1 (2003), [arXiv:cond-mat/9707221](https://arxiv.org/abs/cond-mat/9707221).
- [24] S. Chandrasekharan and U.-J. Wiese, Meron cluster solution of a fermion sign problem, *Phys. Rev. Lett.* **83**, 3116 (1999), [arXiv:cond-mat/9902128](https://arxiv.org/abs/cond-mat/9902128).
- [25] A. B. Zamolodchikov, Integrals of Motion and S Matrix of the (Scaled) T=T(c) Ising Model with Magnetic Field, *Int. J. Mod. Phys. A* **4**, 4235 (1989).
- [26] B. Sriram Shastry and B. Sutherland, Exact ground state of a quantum mechanical antiferromagnet, *Physica B* **108**, 1069 (1981).
- [27] P. Corboz, Y. Zhang, B. Ponsioen, and F. Mila, Quantum spin liquid phase in the shastry-sutherland model revealed by high-precision infinite projected entangled-pair states, preprint (2025), [arXiv:2502.14091 \[cond-mat.str-el\]](https://arxiv.org/abs/2502.14091).
- [28] A. W. Sandvik and H. G. Evertz, Loop updates for variational and projector quantum monte carlo simulations in the valence-bond basis, *Phys. Rev. B* **82**, 024407 (2010).
- [29] H. G. Evertz, G. Lana, and M. Marcu, Cluster algorithm for vertex models, *Phys. Rev. Lett.* **70**, 875 (1993).
- [30] A. W. Sandvik, Ground state projection of quantum spin systems in the valence-bond basis, *Phys. Rev. Lett.* **95**, 207203 (2005).
- [31] C. Destri, F. D. Renzo, E. Onofri, P. Rossi, and G. P. Teccioli, Swendsen-wang monte carlo study of the ising model with external field, *Physics Letters B* **278**, 311 (1992).
- [32] M. Henkel and H. Saleur, The Two-dimensional Ising Model in a Magnetic Field: A Numerical Check of Zamolodchikov's Conjecture, *J. Phys. A* **22**, L513 (1989).
- [33] P. Fonseca and A. Zamolodchikov, Ising spectroscopy. i. mesons at $t < t_c$, preprint (2006), [arXiv:hep-th/0612304 \[hep-th\]](https://arxiv.org/abs/hep-th/0612304).
- [34] J. A. Kjäll, F. Pollmann, and J. E. Moore, Bound states and E_8 symmetry effects in perturbed quantum ising chains, *Phys. Rev. B* **83**, 020407 (2011).
- [35] N. Albert, Y. Zhang, and H.-H. Tu, *Truncated gaussian basis approach for simulating many-body dynamics* (2025), [arXiv:2410.04204 \[cond-mat.str-el\]](https://arxiv.org/abs/2410.04204).
- [36] R. G. Jha, A. Milsted, D. Neuenfeld, J. Preskill, and P. Vieira, Real-time scattering in Ising field theory using matrix product states, *Phys. Rev. Res.* **7**, 023266 (2025), [arXiv:2411.13645 \[hep-th\]](https://arxiv.org/abs/2411.13645).
- [37] A. Litvinov, P. Meshcheriakov, and E. Shestopalov, Meson mass spectrum in ising field theory, *Phys. Rev. D* **112**, 085021 (2025).
- [38] O. F. Syljuåsen, Directed loop updates for quantum lattice models, *Phys. Rev. E* **67**, 046701 (2003).

- [39] T. Nakamura, Vanishing of the negative-sign problem of quantum monte carlo simulations in one-dimensional frustrated spin systems, *Phys. Rev. B* **57**, R3197 (1998).
- [40] A. W. Sandvik, Finite-size scaling of the ground-state parameters of the two-dimensional heisenberg model, *Phys. Rev. B* **56**, 11678 (1997).
- [41] R. A. Sauerwein and M. J. de Oliveira, Ground-state properties of the spin-1/2 antiferromagnetic heisenberg model on a square lattice by a monte carlo method, *Phys. Rev. B* **49**, 5983 (1994).
- [42] W. Zheng, J. Oitmaa, and C. J. Hamer, Phase diagram of the shastry-sutherland antiferromagnet, *Phys. Rev. B* **65**, 014408 (2001).
- [43] M. L. Wagman and M. J. Savage, Taming the Signal-to-Noise Problem in Lattice QCD by Phase Reweighting, preprint (2017), [arXiv:1704.07356 \[hep-lat\]](https://arxiv.org/abs/1704.07356).
- [44] F. Alet, K. Damle, and S. Pujari, Sign-problem-free monte carlo simulation of certain frustrated quantum magnets, *Phys. Rev. Lett.* **117**, 197203 (2016).
- [45] D. Hangleiter, I. Roth, D. Nagaj, and J. Eisert, Easing the monte carlo sign problem, *Science Advances* **6**, eabb8341 (2020), <https://www.science.org/doi/pdf/10.1126/sciadv.abb8341>.
- [46] S. Chandrasekharan, Fermion Bag Approach to Fermion Sign Problems, *Eur. Phys. J. A* **49**, 90 (2013), [arXiv:1304.4900 \[hep-lat\]](https://arxiv.org/abs/1304.4900).
- [47] M. Luscher and P. Weisz, Locality and exponential error reduction in numerical lattice gauge theory, *JHEP* **09**, 010, [arXiv:hep-lat/0108014](https://arxiv.org/abs/hep-lat/0108014).
- [48] C. H. Mak, R. Egger, and H. Weber-Gottschick, Multilevel blocking approach to the fermion sign problem in path-integral Monte Carlo simulations, *Phys. Rev. Lett.* **81**, 4533 (1998), [arXiv:cond-mat/9810002](https://arxiv.org/abs/cond-mat/9810002).
- [49] J. Yoo, S. Chandrasekharan, and H. U. Baranger, A Multi-level algorithm for quantum-impurity models, *Phys. Rev. E* **71**, 036708 (2005), [arXiv:cond-mat/0408123](https://arxiv.org/abs/cond-mat/0408123).